The Astrophysical Journal, 573:7–36, 2002 July 1

GALAXY CLUSTERS IN HUBBLE VOLUME SIMULATIONS: COSMOLOGICAL CONSTRAINTS FROM SKY SURVEY POPULATIONS

A. E. Evrard,[1] T. J. MacFarland,[2,3] H. M. P. Couchman,[4] J. M. Colberg,[5,6] N. Yoshida,[5] S. D. M. White,[5] A. Jenkins,[7] C. S. Frenk,[7] F. R. Pearce,[7,8] J. A. Peacock,[9] and P. A. Thomas[10]
(The Virgo Consortium)
Received 2001 October 26; accepted 2002 March 7

ABSTRACT

We use gigaparticle N-body simulations to study galaxy cluster populations in Hubble volumes of ΛCDM ($\Omega_m = 0.3$, $\Omega_\Lambda = 0.7$) and τCDM ($\Omega_m = 1$) world models. Mapping past light cones of locations in the computational space, we create mock sky surveys of dark matter structure to $z \simeq 1.4$ over 10,000 deg^2 and to $z \simeq 0.5$ over two full spheres. Calibrating the Jenkins mass function at $z = 0$ with samples of ∼1.5 million clusters, we show that the fit describes the sky survey counts to $\lesssim 20\%$ accuracy over all redshifts for systems more massive than poor galaxy groups ($5 \times 10^{13}\ h^{-1}\ M_\odot$). Fitting the observed local temperature function determines the ratio β of specific thermal energies in dark matter and intracluster gas. We derive a scaling with power spectrum normalization $\beta \propto \sigma_8^{5/3}$ and find that the ΛCDM model requires $\sigma_8 = 1.04$ to match $\beta = 1.17$ derived from gasdynamic cluster simulations. We estimate a 10% overall systematic uncertainty in σ_8, 4% arising from cosmic variance in the local sample and the bulk from uncertainty in the absolute mass scale of clusters. Considering distant clusters, the ΛCDM model matches Extended Medium-Sensitivity Survey and *ROSAT* Deep Cluster Survey X-ray–selected observations under economical assumptions for intracluster gas evolution. Using transformations of mass-limited cluster samples that mimic σ_8 variation, we explore Sunyaev-Zeldovich (SZ) search expectations for a 10 deg^2 survey complete above $10^{14}\ h^{-1}\ M_\odot$. Cluster counts are shown to be extremely sensitive to σ_8 uncertainty, while redshift statistics, such as the sample median, are much more stable. Redshift information is crucial to extract the full cosmological diagnostic power of SZ cluster surveys. For ΛCDM, the characteristic temperature at a fixed sky surface density is a weak function of redshift, implying an abundance of hot clusters at $z > 1$. Assuming constant β, one 8 keV cluster at $z > 2$ and 10 5 keV clusters at $z > 3$ are expected in the Sloan Digital Sky Survey area. Too many such clusters can falsify the model; detection of clusters more massive than Coma at $z > 1$ violates ΛCDM at 95% confidence if their surface density exceeds 0.003 deg^{-2}, or 120 on the whole sky.

Subject headings: cosmology: theory — dark matter — galaxies: clusters: general — intergalactic medium
On-line material: color figures, machine-readable tables

1. INTRODUCTION

Studies of galaxy clusters provide a critical interface between cosmological structure formation and the astrophysics of galaxy formation. Spatial statistics of the cluster population provide valuable constraints on cosmological parameters, while multiwavelength studies of cluster content offer insights into the cosmic mix of clustered matter components and the interactions between galaxies and their local environments.

In the near future, the size and quality of observed cluster samples will grow dramatically as surveys in optical, X-ray, and submillimeter wavelengths are realized. In the optical, the ongoing wide-field 2dF Survey (Colless et al. 2001) and the Sloan Digital Sky Survey (SDSS; Kepner et al. 1999; Nichol et al. 2001; Annis et al. 2001) will map the galaxy and cluster distributions over large fractions of the sky to moderate depth ($z \sim 0.3$), while deeper surveys are probing of order tens of square degrees of sky to $z \sim 1$ (Postman et al. 1996; Dalton et al. 1997; Zaritsky et al. 1997; Ostrander et al. 1998; Scoddeggio et al. 1999; Gal et al. 2000; Gladders & Yee 2000; Willick et al. 2001; Gonzalez et al. 2001). In the X-ray, *ROSAT* archival surveys (Scharf et al. 1997; Rosati et al. 1998; Ebeling et al. 1998; Viklihnin et al. 1998; de Grandi et al. 1999; Romer et al. 2000; Böhringer et al. 2001; Ebeling, Edge, & Henry 2001; Gioia et al. 2001) have generated redshift samples of many hundreds of clusters. Similar surveys to come from developing *Chandra* and *XMM* archives (see, e.g., Romer et al. 2001) will lead to order-of-magnitude improvements in sample size and limiting sensitivity. Finally, the detection of clusters via their spectral imprint on the microwave background (Sunyaev & Zeldovich 1972; Birkinshaw 1999) offers a new mode of efficiently surveying for very distant ($z > 1$) clusters with hot, intracluster plasma (Barbosa et al. 1996; Holder et al. 2000; Kneissl et al. 2001).

[1] Departments of Physics and Astronomy, University of Michigan at Ann Arbor, 830 Dennison, 501 East University Avenue, Ann Arbor, MI 48109-1120.
[2] Rechenzentrum Garching, Boltzmannstrasse 2, D-85740 Garching, Germany.
[3] 1Click Brands LLC, 704 Broadway, New York, NY 10003.
[4] Department of Physics and Astronomy, McMaster University, Hamilton, ON L8S 4M1, Canada.
[5] Max-Planck-Institut für Astrophysik, Karl-Schwarzschild-Strasse 1, D-85740 Garching, Germany.
[6] Econovo Software, 1 State Street, Boston MA 02109.
[7] Department of Physics, Durham University, South Road, Durham DH1 3LE, UK.
[8] Department of Physics and Astronomy, University of Nottingham, Nottingham NG7 2RD, UK.
[9] Institute for Astronomy, University of Edinburgh, Royal Observatory, Edinburgh EH9 3HJ, UK.
[10] Astronomy Centre, CEPS, University of Sussex, Brighton BN1 9QJ, UK; evrard@umich.edu.

Deciphering the cosmological and astrophysical information in the coming era of large survey data sets requires the ability to accurately compute expectations for observables within a given cosmology. Given some survey observation R at redshift z, a likelihood analysis requires the probability $p(R, z|\mathscr{C}, \mathscr{A})$ that such data would arise within a model described by sets of cosmological $\mathscr{C} \equiv C_i$ and astrophysical $\mathscr{A} \equiv \{A_j\}$ parameters. Considering clusters as nearly a one-parameter family ordered by total mass M, the likelihood of the observable R can be written

$$p(R, z|\mathscr{C}, \mathscr{A}) = \frac{\int dM\, p(M, z|\mathscr{C}) p(R|M, z, \mathscr{A})}{\int dM\, p(M, z|\mathscr{C})} \ , \quad (1)$$

where $p(M, z|\mathscr{C})$ is the likelihood that a cluster of mass M exists at redshift z in cosmology $\mathscr{C}$ within the survey of interest and $p(R|M, z, \mathscr{A})$ is the likelihood that observable R is associated with such a cluster given the astrophysical model $\mathscr{A}$.

Separating the problem in this way assumes its pieces to be independent. The space density $n(M, z|\mathscr{C})$, or *mass function*, describes the probability of finding a cluster at redshift z with total mass M within comoving volume element dV:

$$p(M, z|\mathscr{C}) \propto n(M, z|\mathscr{C}) dV \ . \quad (2)$$

The absence of explicit astrophysical dependence in the mass function is based on the assumption that weakly interacting dark matter dominates the matter energy density. If a cluster's total mass M is relatively immune to astrophysical processes, then the mass function can be well determined independently of $\mathscr{A}$. On the other hand, the likelihood of a particular observable feature $p(R|M, z, \mathscr{A})$ is dependent, often critically, on the astrophysical model. For optical and X-ray observations in particular, it encapsulates the answer to the question "how do dark matter potential wells light up?"

For Gaussian initial density fluctuation spectra, Press & Schechter (1974, hereafter PS) used a spherical collapse argument and N-body simulation to show that the space density of the rarest clusters is exponentially sensitive to the amplitude of density perturbations on $\sim 10\ h^{-1}$ Mpc scales. The analytic form of PS was put on a more rigorous footing by Bond et al. (1991), but recent extensions to ellipsoidal collapse (Sheth & Tormen 1999; Lee & Shandarin 1999) revise the original functional form. Calibration by N-body simulations has led to a functional shape for the mass function that retains the essential character of the original PS derivation (Jenkins et al. 2001, hereafter J01, and references therein). For cluster masses defined using threshold algorithms tied to the cosmic mean mass density $\bar{\rho}_m(z)$, J01 show that the mass fraction in collapsed objects is well described by a single function that depends only on the shape of the filtered power spectrum of initial fluctuations $\sigma^2(M)$.

Complications arise in determining the mass function $n(M, z)$ from both simulations and observations. The first is semantic. Clusters formed from hierarchical clustering do not possess unique, or even distinct, physical boundaries, so it is not obvious what mass to assign to a particular cluster. This issue is solvable by convention, and we choose here a commonly employed measure M_Δ, defined as the mass interior to a sphere within which the mean density is a fixed multiple Δ of the critical density $\rho_c(z)$ at the epoch of identification z. Acknowledging the nonunique choice of threshold, we develop in Appendix B a model, based on the mean density profile of clusters derived from simulations (Navarro, Frenk, & White 1996, 1997), that transforms the mass function fit parameters to threshold values different from those used here.

Attempts to empirically constrain the mass function are complicated by the inability to directly observe the theoretically defined mass. Instead, a surrogate estimator $\hat{M}$ must be employed that is, in general, a biased and noisy representation of M_Δ. For example, estimates derived from the weak gravitational lensing distortions induced on background galaxies tend to overestimate M_Δ by $\sim$20%, with a dispersion on the order of unity (Metzler, White, & Loken 2001; White, van Waerbeke, & Mackey 2001).

The temperature T of the intracluster medium (ICM) derived from X-ray spectroscopy is an observationally accessible mass estimator. Gasdynamic simulations predict that the ICM rarely strays far from virial equilibrium (Evrard 1990; Evrard, Metzler, & Navarro 1996; Bryan & Norman 1998; Yoshikawa, Jing, & Suto 2000; Mathiesen & Evrard 2001), so that $p(M|T)$ is well described by a mean power-law relation with narrow ($\lesssim$15% in mass) intrinsic scatter. Observations are generally supportive of this picture (Hjorth, Oukbir, & van Kampen 1998; Mohr, Mathiesen, & Evrard 1999; Horner, Mushotzky, & Scharf 1999; Nevalainen, Markecitch, & Forman 2000), but the detailed form of $p(M|T)$ remains uncertain. The overall normalization is a particular concern; we cannot prove that we know the median mass of, say, a 6 keV cluster to better than 25% accuracy.

Even with this degree of uncertainty, the space density of clusters as a function of T (the *temperature function*) has been used to place tight constraints on σ_8, the present, linearly evolved amplitude of density fluctuations averaged within spheres of radius $8\ h^{-1}$ Mpc. Henry & Arnaud (1991) derived $\sigma_8 = 0.59 \pm 0.02$ from temperatures of 25 clusters in a bright, X-ray flux-limited sample, assuming $\Omega_m = 1$. Subsequent analysis of this sample (White, Efstathiou, & Frenk 1993; Eke, Cole, & Frenk 1996; Vianna & Liddle 1996; Fan, Bahcall, & Cen 1997; Kitayama & Suto 1997; Pen 1998) and revised samples (Markevitch 1998; Blanchard et al. 2000) generated largely consistent results and extended constraints to arbitrary Ω_m. For example, Pierpaoli, Scott, & White (2001, hereafter PSW), reanalyzing the Markevitch sample using revised temperatures of White (2000), find

$$\sigma_8 = 0.495^{+0.034}_{-0.037} \Omega_m^{-0.60} \ . \quad (3)$$

Accurate determination of σ_8 is a prerequisite for deriving constraints on the clustered mass density Ω_m from a differential measurement of the local and high-redshift cluster spatial abundances. Most studies have excluded the possibility that $\Omega_m = 1$ from current data (Luppino & Kaiser 1997; Bahcall, Fan, & Cen 1997; Carlberg, Yee, & Ellingson 1997; Donahue et al. 1998; Eke et al. 1998; Bahcall & Fan 1998), but others disagree (Sadat, Blanchard, & Oukbir 1998; Blanchard & Barlett 1998; Vianna & Liddle 1999). Uncertainty in σ_8 plays a role in this ambiguity, as recently illustrated by Borgani et al. (1999a). In their analysis of 16 CNOC clusters at redshifts $0.17 \leq z \leq 0.55$, the estimated value of Ω_m shifts by a factor of 3, from 0.35 to 1.05, as σ_8 is varied from 0.5 to 0.6.

Motivated by the need to study systematic effects in both local and distant cluster samples, we investigate the spatial

distribution of clusters in real and redshift space samples derived from N-body simulations of cosmic volumes comparable in scale to the Hubble volume $(c/H_0)^3$. A pair of 10^9 particle realizations of flat cold dark matter (CDM) cosmologies are evolved with particle mass equivalent to that associated with the extended halos of bright galaxies. The simulations are designed to discover the rarest and most massive clusters (by maximizing volume) while retaining force and mass resolution sufficient to determine global quantities (mass, shape, low-order kinematics) for objects more massive than poor groups of galaxies ($\sim 5 \times 10^{13}\ h^{-1}\ M_\odot$). To facilitate comparison to observations, we generate output that traces the dark matter structure along the past light cone of two observing locations within the computational volume. These virtual *sky surveys*, along with usual fixed proper time *snapshots*, provide samples of millions of clusters that enable detailed statistical studies. We publish the cluster catalogs here as electronic tables.

In this paper we extend the detailed cluster mass function analysis of J01 to the sky survey output, updating results using a cluster-finding algorithm with improved completeness properties for poorly resolved groups. We match the observed local X-ray temperature function by tuning the proportionality factor β between the specific energies of dark matter and intracluster gas. The required value of β depends on the assumed σ_8, and we derive a scaling $\beta \sim \sigma_8^{5/3}$ based on virial equilibrium and the Jenkins mass function (JMF) form. From $z = 0$ subvolumes sized to local temperature samples, we show that sample variance of temperature-limited samples contributes $\sim$4% uncertainty to determinations of σ_8. Uncertainty in converting temperatures to masses remains the dominant source of systematic error in σ_8, and we investigate the influence of a 25% uncertainty in mass scale on expectations for Sunyaev-Zeldovich (SZ) searches.

In § 2 we describe the simulations, including the process of generating sky survey output, and the model used to convert dark matter properties to X-ray observables. The cluster mass function is examined in § 3. Million cluster samples at $z = 0$ are used to determine the best-fit parameters of the JMF, and we show that this function reproduces well the sky survey populations extending to $z > 1$. The interplay between the fit parameters, σ_8, and the normalization of cluster masses is explored, and this motivates a procedure for transforming the discrete cluster sets to mimic variation in σ_8.

In § 4 we use observations analyzed by PSW to calibrate the specific energy factor β for each model. We explore properties of the high-redshift cluster population in § 5, emphasizing uncertainties from σ_8 error, intracluster gas evolution, and possible X-ray selection biases under low signal-to-noise conditions. The σ_8 transformations developed in § 3 are used to explore cluster yields anticipated from upcoming SZ surveys, and the median redshift in mass-limited samples is identified as a robust cosmological discriminant. Characteristic properties of the ΛCDM cluster population are summarized in § 6, and we review our conclusions in § 7.

2. HUBBLE VOLUME SIMULATIONS

After an upgrade in 1997 of the Cray T3E at the Rechenzentrum Garching[11] to 512 processors and 64 Gbytes of memory, we carried out a pair of one billion (10^9) particle Hubble volume (HV) simulations over the period 1997 October to 1999 February. A memory-efficient version of the Couchman, Pearce, and Thomas Hydra N-body code (Pearce & Couchman 1997) parallelized using "shmem" message-passing utilities was used to perform the computations. MacFarland et al. (1998) provide a description and tests of the parallel code.

We explore two cosmologies with a flat spatial metric, a ΛCDM model dominated by vacuum energy density (a nonzero cosmological constant) and a τCDM model dominated by nonrelativistic, cold dark matter. The τCDM model was completed in 1998 May, while the ΛCDM model was finished in 1999 February. Published work from these simulations includes an extensive analysis of counts-in-cells statistics (to >10th order) by Colombi et al. (2000) and Szapudi et al. (2000), investigation of the clustering behavior of clusters (Colberg et al. 2000; Padilla & Baugh 2002), analysis of two-point function estimators (Kerscher, Szapudi, & Szalay 2000), a description of the mass function of dark matter halos (J01), a study of confusion on the X-ray sky due to galaxy clusters (Voit, Evrard, & Bryan 2001), and statistics of pencil beam surveys (Yoshida et al. 2001). Kay, Liddle, & Thomas (2001) use the sky survey catalogs to predict SZ signatures for the planned *Planck Surveyor* mission, while Outram et al. (2001) use the deep mock ΛCDM surveys to test analysis procedures for the 2dF QSO Redshift Survey.

2.1. *Simulation Description*

Table 1 summarizes parameter values for each model, including the final epoch matter density Ω_m, vacuum energy density Ω_Λ, power spectrum normalization σ_8, starting redshift $z_{\rm init}$, simulation side length L, and particle mass m.

Values of σ_8 were chosen to agree approximately with both the amplitude of temperature anisotropies in the cosmic microwave background as measured by *COBE* and the nearby space density of rich X-ray clusters. The degree of uncertainty in these constraints allows the final space density of clusters as a function of mass to differ between the two simulations. However, as we discuss below, it is possible to ensure that the observed space density of clusters as a function of X-ray temperature is matched in both models by adjusting a free factor β used to link X-ray temperature to dark matter velocity dispersion.

To initiate the numerical experiments, particle positions and momenta at $z_{\rm init}$ are generated by perturbing a replicated "glass" of one million particles with a set of discrete waves randomly drawn from power spectra computed for each cosmology. Initial Fourier modes of the applied perturbations have amplitudes drawn from a Gaussian distribution with variance given by the power spectrum $P(k) = T(k)P_{\rm prim}(k)$. A Harrison-Zeldovich primordial

TABLE 1
MODEL PARAMETERS

Model	Ω_m	Ω_Λ	σ_8	$z_{\rm init}$	L[a] (h^{-1} Mpc)	m[b] ($\times 10^{12}\ h^{-1}\ M_\odot$)
ΛCDM.....	0.3	0.7	0.9	35	3000	2.25
τCDM	1.0	0	0.6	29	2000	2.22

[a] Cube side length.
[b] Particle mass.

[11] The Max-Planck Society Computing Center at Garching.

spectrum $P_{\rm prim}(k) \propto k$ is assumed for both models. For the ΛCDM model, the transfer function $T(k)$ is computed using CMBFAST (Seljak & Zaldarriaga 1996) assuming $h = 0.7$ and baryon density $\Omega_b h^2 = 0.0196$ (Burles & Tytler 1998). The τCDM model uses transfer function $T(k) = \{1 + [aq + (bq)^{3/2} + (cq)^2]^\nu\}^{-1/\nu}$, where $q = k/\Gamma$, $\Gamma = \Omega_m h$, $a = 6.4\ h^{-1}$ Mpc, $b = 3\ h^{-1}$ Mpc, $c = 1.7\ h^{-1}$ Mpc, and $\nu = 1.13$ (Bond & Efstathiou 1984).

The simulations are designed to resolve the collapse of a Coma-sized cluster with 500 particles. Although this resolution is sufficient to capture only the later stages of the hierarchical buildup of clusters, convergence tests (Moore et al. 1998; Frenk et al. 1999) show that structural properties on scales larger than a few times the gravitational softening length are essentially converged. From tests presented in J01 and in Appendix A, cluster identification is robust down to a level of about 20 particles. Using $M_{\rm Coma} = 1.1 \times 10^{15}\ h^{-1}\ M_\odot$ (White et al. 1993) leads to particle mass $2.2 \times 10^{12}\ h^{-1}\ M_\odot$ in both models, comparable to the total mass within $\sim 300\ h^{-1}$ kpc of bright galaxies (Fischer et al. 2000; Smith et al. 2001; Wilson, Kaiser, & Luppino 2001). The mass associated with one billion particles at the mean mass density sets the length L of the periodic cube used for the computations, resulting in a Hubble length $L = c/H_0 = 3\ h^{-1}$ Gpc for the ΛCDM model and $L = 2\ h^{-1}$ Gpc for τCDM.

A Newtonian description of gravity is assumed, appropriate for weak-field structures. A nonretarded gravitational potential is employed because the peculiar acceleration converges on scales well below the Hubble length. The good agreement between the higher order clustering statistics of the simulations and expectations derived from an extended perturbation theory treatment of mildly nonlinear density fluctuations provides indirect evidence that this treatment of gravity is accurate (Colombi et al. 2000; Szapudi et al. 2000).

Gravitational forces on each particle are calculated as a sum of a long-range component, determined on a uniform spatial grid of 1024^3 elements using fast Fourier transforms, and a short-range component found by direct summation. The latter force is softened with a spline smoothing roughly equivalent to a Plummer law gravitational potential $\phi(r) \propto (r^2 + \varepsilon^2)^{-1/2}$ with smoothing scale $\varepsilon = 0.1\ h^{-1}$ Mpc. A leapfrog time integration scheme is employed with 500 equal time steps for each calculation.

Processor time for these computations was minimized by employing a parallel algorithm well matched to the machine architecture (MacFarland et al. 1998) and by simulating large volumes that entail a minimum of message passing overhead. The Cray T3E offers high interprocessor communication bandwidth along with a native message-passing library ("shmem") to control data flow. A two-dimensional, block-cyclic domain decomposition scheme allocates particles to processors. Each processor advances particles lying within a disjoint set of rectangular regions of dimension $L \times (L/32) \times (L/16)$ that subdivides the computational space. Each calculation required approximately 35,000 processor hr, or 3 days of the 512 processor machine. This corresponds to advancing roughly 4000 particles s^{-1} on an average step. The computations were essentially limited by I/O bandwidth rather than CPU speed. Execution was performed in roughly 20 stages spanning a calendar time of 3–4 months, with data archived to a mass storage system between stages. Approximately 500 Gbytes of raw data were generated by the pair of simulations.

2.2. *Sky Survey Output*

In addition to the traditional simulation output of snapshots of the particle kinematic state at fixed proper time, we introduce here sky survey output that mimics the action of collecting data along the past light cone of hypothetical observers located within the simulation volume. The method extends to wide-angle surveys an approach pioneered by Park & Gott (1991) in simulating deep, pencil beam observations. Since there is no preferred location in the volume, we chose two survey origins, located at the vertex and center of the periodic cube for convenience.

In a homogeneous world model, a fixed observer at the present epoch t_0 receives photons emitted at $t < t_0$ that have traversed comoving distances $r(t) = c \int_t^{t_0} dt\, a^{-1}(t)$, where $a(t)$ is the scale factor of the metric [$a(t_0) = 1$] and c the speed of light. The set of events lying along the continuum of concentric spheres t, $\boldsymbol{r}(t)$ for $t < t_0$ defines the past light cone of that observer. In the discrete environment of the numerical simulation, we construct the light cone survey by choosing spherical shells of finite thickness such that each particle's state is saved at a pair of consecutive time steps that bound the exact time of intersection of the light cone with that particle's trajectory. Defining t_i as the proper time at step i of the computation, we choose inner and outer radii $(1 - \eta) r(t_{i+1})$ and $(1 + \eta) r(t_{i-1})$. Here $\eta \simeq 0.02$ is a small parameter that safeguards against a particle appearing only once in the output record because of peculiar motion across the discrete shells during a step. The inner radius is set to zero on the final two steps of the computation.

With successive states for particles in the output record, a linear interpolation is performed to recover the original second-order time accuracy of the leapfrog integrator. Given a particle's position relative to the survey origin $\boldsymbol{x}_i$ and, at the subsequent step, $\boldsymbol{x}_{i+1} \equiv \boldsymbol{x}_i + \Delta\boldsymbol{x}$, we solve for interpolation parameter α defining position $\boldsymbol{x} = \boldsymbol{x}_i + \alpha\, \Delta\boldsymbol{x}_i$ such that $|\boldsymbol{x}| = r(t_i + \alpha\, \Delta t)$, with Δt the time step. For a spherical survey, this implies

$$\alpha = \frac{r^2(t_i) - x_i^2}{2[\boldsymbol{x}_i \cdot \Delta\boldsymbol{x} + r(t_i)\Delta r]}\ , \tag{4}$$

with $\Delta r = r(t_i) - r(t_{i+1}) > 0$. After solving for α, the particle's position and velocity are interpolated and the result stored to create the processed sky survey data sets. Comoving coordinates and physical velocities are stored as 2 byte integers, sufficient to provide $\sim \varepsilon/10$ positional accuracy and kilometer per second accuracy in velocity. Data are stored in binary form in multiple files, each covering a spatial subcube of side $L/16$ of the entire computational volume.

The scale L, along with the comoving distance-redshift relations shown in Figure 1, determine the redshift extents of the surveys listed in Table 2. Two principal survey types—spheres and octants—extend to distances $L/2$ and L, respectively. From the cube center, the MS full-sphere surveys extend to redshifts $z_{\rm max} = 0.57$ (ΛCDM) and 0.42 (τCDM). From the origin and its diagonally opposite image, octant surveys (PO and NO) extend to redshifts 1.46 (ΛCDM) and 1.25 (τCDM), respectively. The surveys have opposite orientation; both viewing the interior region of the computational space. The VS sphere centered on the origin is created using translational symmetries of separate octant surveys conducted from the eight vertices of the fundamental cube. The interior portions of the PO and NO surveys

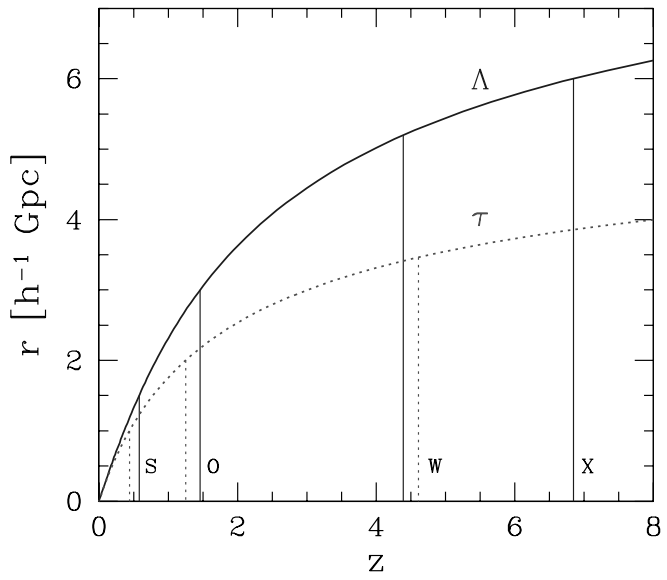

FIG. 1.—Comoving look-back distance as a function of redshift for ΛCDM (*solid line*) and τCDM (*dashed line*). The vertical lines indicate redshift limits of the spherical (S), octant (O), deep wedge (W), and extended wedge (X) surveys (Table 2). [*See the electronic edition of the Journal for a color version of this figure.*]

are thus subsets (opposite caps) of the VS survey. The combined volumes of the spheres and octants sample the computational volume roughly once for each type. In terms of cosmic time, the octants extend over the last 74% and 71% of the age of the universe (ΛCDM and τCDM, respectively), equivalent to roughly a 10 Gyr look-back time.

In addition to these surveys, smaller solid angle wedge surveys reach to greater depth. A 10×10 deg^2 deep wedge (DW) extends along the cube diagonal to the opposite corner and reaches redshifts 4.4 (ΛCDM) and 4.6 (τCDM). For the ΛCDM model only, a 16×76 deg^2 extended wedge (XW) uses periodic images of the fundamental cube to reach $z_{\max} = 6.8$. This wedge is a partial extension of the PO survey.

2.3. *Connecting to X-Ray Observations*

Connecting to observations of clusters requires a model that relates luminous properties to the underlying dark matter. We focus here on the ICM temperature T under the assumption that both T and the dark matter velocity dispersion σ_v are related to the underlying dark matter gravitational potential through the virial theorem (Cavaliere & Fusco-Femiano 1976). Empirical support for this assumption comes from the observation that $T \sim \sigma_{\rm gal}^2$ (see, e.g., Wu, Xue, & Fang 1999), the scaling expected if both galaxies and the ICM are thermally supported within a common potential. High-resolution simulations of galaxy formation within a cluster indicate that $\sigma_{\rm gal}$ should accurately reflect the dark matter σ_v except for the brightest, early-type galaxies, which display a mild bias toward lower velocity dispersion (Springel et al. 2001).

Rather than map T to M directly, we prefer to use a one-to-one mapping between T and dark matter velocity dispersion σ_v. This approach has the advantage of naturally building in scatter between T and M at a fractional amplitude $\sim$10% that is consistent with expectations from direct, gasdynamic modeling (see, e.g., Mathiesen & Evrard 2001; Thomas et al. 2001). Define a one-dimensional velocity dispersion σ_v by

$$\sigma_v^2 = \frac{1}{3N_p} \sum_{i=1}^{N_p} \sum_{j=1}^{3} |v_{i,j} - \bar{\boldsymbol{v}}_j|^2 \ , \qquad (5)$$

where the index i ranges over the N_p cluster members identified within r_Δ, j sums over principal directions, and $\bar{\boldsymbol{v}}$ is the mean cluster velocity defined by the same N_p members. We assume that σ_v^2 maps directly to X-ray temperature and introduce as an adjustable parameter the ratio of specific energies $\beta \equiv \sigma_v^2/(kT/\mu m_p)$, where k is Boltzmann's constant, μ the mean molecular weight of the plasma (taken to be 0.59), and m_p the proton mass. We fit β by requiring that the models match the local temperature function.

Varying the power spectrum normalization σ_8 leads to shifts in the space density of clusters as a function of mass and velocity dispersion. Values of β required to fit X-ray observations thus depend on σ_8, and we derive an approximate form for this dependence in § 4.4.

TABLE 2
LIGHT CONE SKY SURVEYS

Name	Center	Solid Angle	$z_{\max}(\Lambda)$	$z_{\max}(\tau)$
MS.....	$(L/2, L/2, L/2)$	4π	0.57	0.42
VS.....	(0, 0, 0)	4π	0.57	0.42
PO[a]	(0, 0, 0)[b]	$\pi/2$	1.46	1.25
NO[a]	(L, L, L)[b]	$\pi/2$	1.46	1.25
DW.....	(0, 0, 0)[b]	$10^\circ \times 10^\circ$	4.4	4.6
XW.....	(0, 0, 0)	$16^\circ \times 76^\circ$	6.8	...

[a] NO and PO have opposite orientations about a common center.
[b] Orientation centered on cube diagonal.

3. CLUSTER POPULATIONS

We begin this section by visualizing the evolution of clustering in the octant surveys. Details of the cluster-finding algorithm are then presented and fits to the $z = 0$ mass functions performed for $\Delta = 200$. A simple model for evolving the fit parameters with redshift in the ΛCDM case is given and predictions based on the $z = 0$ fits compared to the sky survey output in three broad redshift intervals.

Additional details are provided in two appendices. Appendix A compares output of the SO algorithm employed here to that used by J01. Appendix B presents a model for extending the mass function fits under variation of the density threshold Δ. More generally, it provides a means to transform the discrete cluster sample under variation of σ_8. Appendix C presents the sky survey and $z = 0$ cluster catalogs as electronic tables. Truncated versions in the print edition list the 10 most massive clusters in each survey. Electronic versions list all clusters above a mass limit of $5 \times 10^{13}\, h^{-1}\, M_\odot$ (22 particles).

3.1. *Evolution of the Matter Distribution*

In Figure 2 we present maps of the Lagrangian smoothed mass density in slices through the octant surveys that extend to $z = 1.25$. Horizontal and vertical maps show comoving

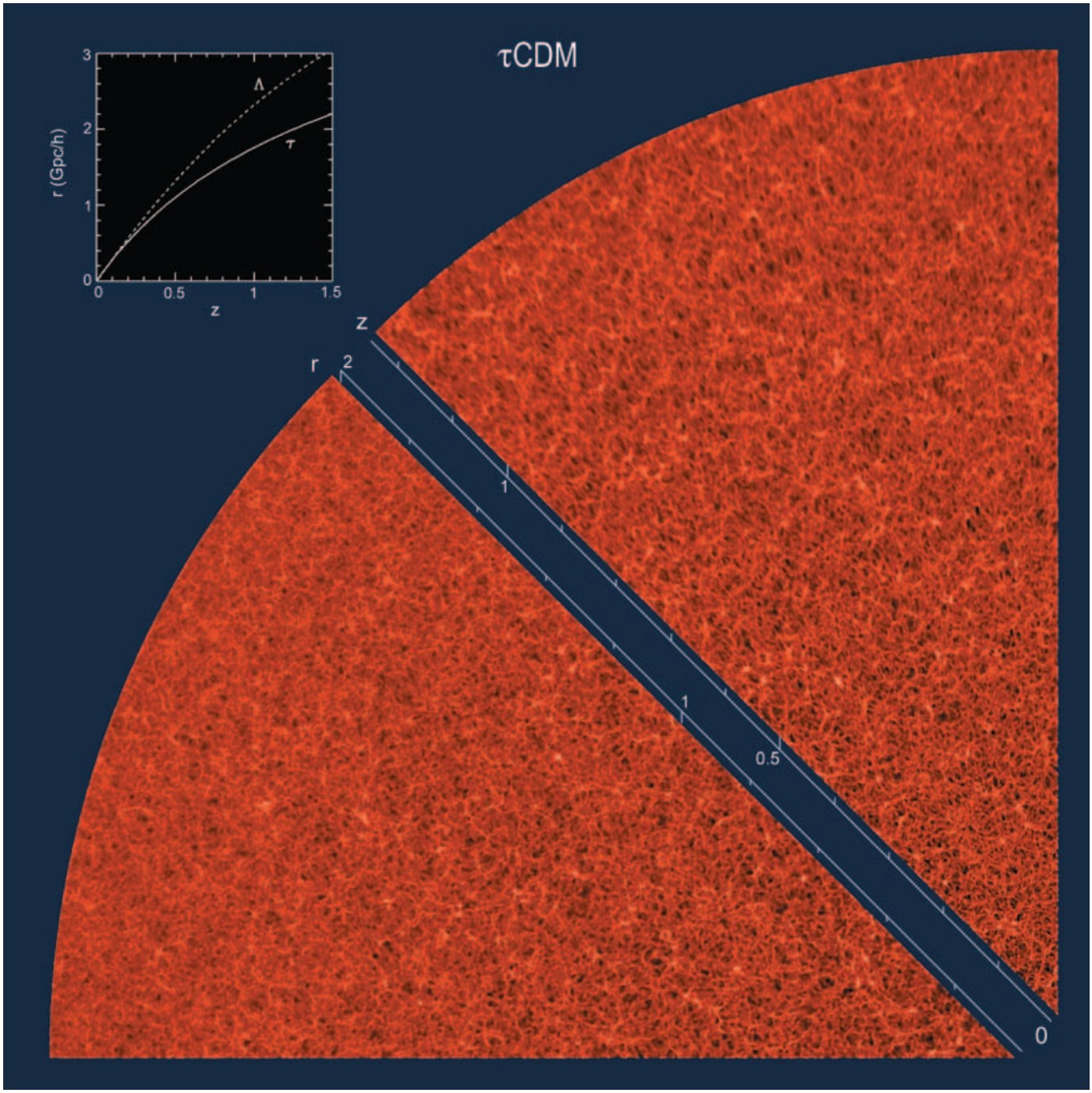

FIG. 2*a*

FIG. 2.—Maps of the dark matter in slices through the deep octant surveys in (*a*) τCDM and (*b*) ΛCDM world models. Survey origins are at the vertices (O), and color represents mass density relative to the mean ranging from 0.05 (*black*) to 50 (*white*) on a logarithmic scale. Density is mapped onto a two-dimensional grid using an adaptive (Lagrangian) smoothing kernel with scale $2 \times 10^{13}\ h^{-1}\ M_{\odot}$. For each model, two representations of a 45° slice extending to $z = 1.25$ are shown. The horizontal maps display structure in the comoving metric, while the vertical maps display the same comoving region, reflected about the diagonal, in redshift space. Positions of clusters at the intersection of filaments are evident in redshift space through the radial distortions arising from their internal velocity dispersions (so-called fingers of God). The inset of the τCDM image shows the relation between comoving distance r and redshift z over the range mapped by the images. The inset of the ΛCDM image shows a close-up of the particle distribution around the largest cluster of the ΛCDM octant surveys, located at $z = 1.04$. Particles colored white lie within a sphere of physical radius $1.5\ h^{-1}$ Mpc that encompasses a mean density 200 times the critical value.

and redshift space representations, respectively. Since the Hubble length far exceeds the characteristic clustering length of the mass, the feature most immediately apparent in the density maps is their overall homogeneity. Gravitational enhancement of the clustering amplitude over time is evident from the fact that the density fluctuations are more pronounced near the survey origin (vertex of each triangular slice) compared to the edge. The effect is subtle in this image because the dynamic range in density, from black to white, spans 3 orders of magnitude, much larger than the linear

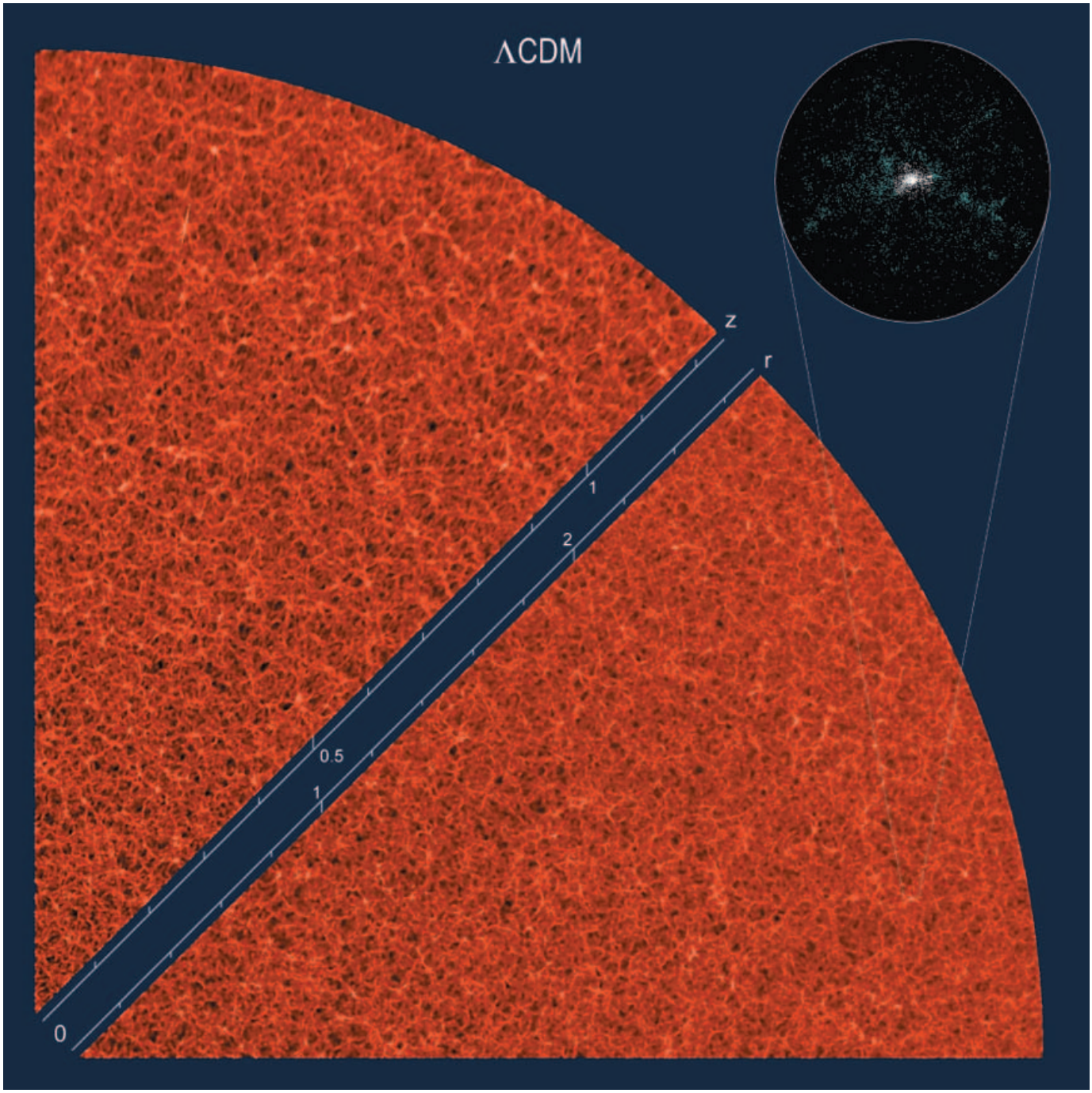

FIG. 2*b*

growth factors of 1.8 (ΛCDM) and 2.2 (τCDM) for large-scale perturbations in the interval shown.

To verify the accuracy of the clustering evolution in the octant surveys, we show in Figure 3 the behavior of the rms amplitude of density fluctuations $\langle \delta^2 \rangle^{1/2}$, where $\delta \equiv \rho/\bar{\rho}_m(z) - 1$, within spheres encompassing, on average, a mass of $2.2 \times 10^{15}\ h^{-1}\ M_\odot$ (1000 particles). Points in the figure show $\langle \delta^2 \rangle^{1/2}$ determined by randomly sampling locations within 20 radial shells of equal volume in the octant surveys. Values are plotted at the volume-weighted redshift of each shell. Solid lines are not fits but show the expectations for $\langle \delta^2 \rangle^{1/2}$ based on linear evolution of the input power spectrum. Deviations between the measured values and linear theory, shown in the upper panels of Figure 3, are at the 1% level. Although we do not attempt here to model these deviations explicitly, Szapudi et al. (2000) show that the higher-order clustering properties of these simulations at the final epoch are well described by an extended perturbation theory treatment of fluctuation evolution.

The orientation of the slice shown in Figure 2 is chosen to include the most massive cluster in the ΛCDM octant surveys. It lies at the surprisingly high redshift $z = 1.04$. The inset of Figure 2*b* shows that this cluster is actively forming from mergers fed by surrounding filaments. In Figure 4 we

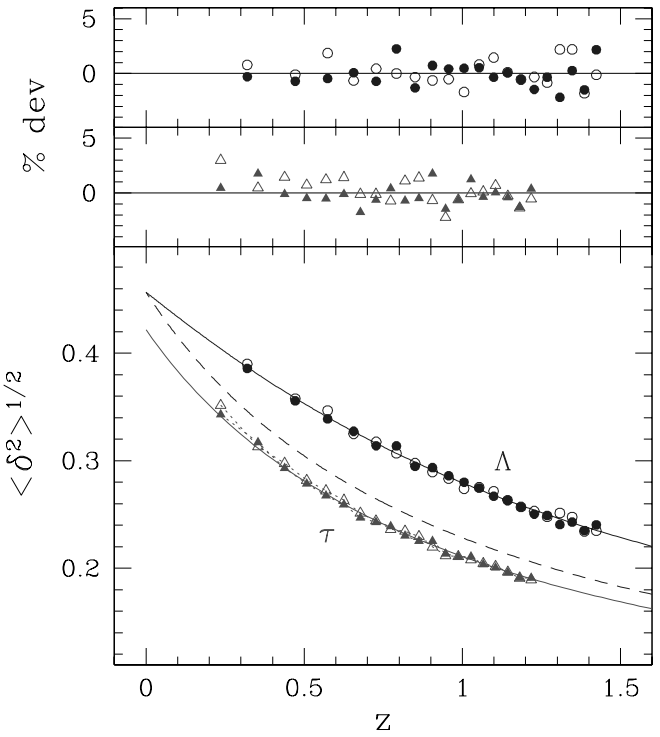

FIG. 3.—Redshift evolution of the rms amplitude of density fluctuations $\langle\delta^2\rangle^{1/2}$ in top-hat spheres containing, on average, a mass of $2.2 \times 10^{15}\ h^{-1}\ M_\odot$ (1000 particles). The symbols are octant survey measurements (*filled symbols*: PO; *open symbols*: NO) from the ΛCDM (*circles*) and τCDM (*triangles*) simulations, obtained by randomly sampling 20 radial shells of equal comoving volume and plotted at the volume-weighted redshift of each shell. The solid lines are predictions from linear theory based on the input fluctuation spectra. The upper panel demonstrates agreement with linear theory at the ∼1% level, except for the nonlinear departure of τCDM fluctuations at late times. The dashed line in the lower panel shows the evolution that ΛCDM fluctuations would have if they followed the τCDM linear growth evolution. [*See the electronic edition of the Journal for a color version of this figure*.]

show a close-up of the redshift space structure in 75,000 km s^{-1} wide regions centered at $z = 1.1$ and lying just interior to the vertical edges of the redshift space views of Figure 2. The gray scale shows only overdense material $\delta > 0$, and the region includes the most massive ΛCDM cluster. With a rest-frame line-of-sight velocity dispersion of 1964 km s^{-1}, it produces a ∼16,000 km s^{-1} sized "finger-of-God" feature in the lower right-hand image.

Along with this extreme object, close inspection of Figure 4 reveals many more smaller fingers representing less massive clusters in the ΛCDM image. The τCDM panel contains many fewer such clusters. It is this difference that motivates high-redshift cluster counts as a sensitive measure of the matter density parameter Ω_m. To perform quantitative analysis of the cluster population, we first describe the method used to identify clusters in the particle data sets.

3.2. *Cluster-Finding Algorithm*

A number of methods have been developed for identifying clusters within the particle data sets of cosmological simulations. We refer the reader to J01, White (2001), and Lacey & Cole (1994) for discussion and intercomparisons of common approaches. Two algorithms are employed by J01. One is a percolation method known as "friends-of-friends" (FOF) that identifies a group of particles whose members have at least one other group member lying closer than some threshold separation. The threshold separation, typically expressed as a fraction η of the mean interparticle spacing, is a parameter whose variation leads to families of groups, referred to as FOF(η), with favorable nesting properties (Davis et al. 1985).

The other algorithm of J01 is a spherical overdensity (SO) method that identifies particles within spheres, centered on local density maxima, having radii defined by a mean enclosed isodensity condition. We use here an SO algorithm that differs slightly from that of J01. The isodensity condition requires the mean mass density within radius r_Δ to be a factor Δ times the critical density $\rho_c(z)$ at redshift z. J01 define spherical regions that are overdense with respect to the mean background, rather than critical, mass density. For clarity, we refer to the approaches as "mean SO" and "critical SO" algorithms. If not stated explicitly, reference to SO(Δ) should be read as the critical case evaluated at contrast Δ. By definition, a critical SO(Δ) population is identical to a mean SO(Δ/Ω_m) population.

Our method employs a code independent of that used by J01. The codes produce matching output for well-resolved groups but differ at low particle number. Appendix A provides a discussion of completeness based on direct comparison of group catalogs from the algorithms.

3.3. *Mass Function Fits at $z = 0$*

By co-adding 22 snapshots of 11 Virgo consortium simulations ranging in scale from 84.5 to 3000 h^{-1} Mpc, J01 showed that the space density of clusters defined by either FOF(0.2) or SO(180) algorithms are well described by a single functional form when expressed in terms of $\ln\sigma^{-1}(M)$, where $\sigma^2(M)$ is the variance of the density field smoothed with a spherical top-hat filter enclosing mass M at the mean density. Define the mass fraction $f(\ln\sigma^{-1})$ by

$$f\left(\ln\sigma^{-1}\right) \equiv \frac{M}{\bar{\rho}_m(z)}\frac{dn(<M, z)}{d\ln\sigma^{-1}}\ , \qquad (6)$$

with $\bar{\rho}_m(z)$ the background matter density at the epoch of interest and $n(<M, z)$ the cumulative number density of clusters of mass M or smaller. The general form found by J01 for the mass function is

$$f\left(\ln\sigma^{-1}\right) = A\exp\left(-|\ln\sigma^{-1} + B|^\epsilon\right)\ , \qquad (7)$$

where A, B, and ϵ are fit parameters. The amplitude A sets the overall mass fraction in collapsed objects, e^B plays the role of a (linearly evolved) collapse perturbation threshold, similar to the parameter δ_c in the Press-Schechter model or its variants, and ϵ is a stretch parameter that provides the correct shape of the mass function at the very dilute limit.

Values of these parameters depend on the particular cluster-finding scheme implemented, but J01 show them to be independent of cosmology and redshift when cluster masses are based on algorithms tied to the mean mass density. For the FOF(0.2) group catalogs, J01 find that $A = 0.315$, $B = 0.61$, and $\epsilon = 3.8$ provide a fit that describes all of the numerical data to $\lesssim$20% precision over 8 orders of magnitude in number density.

We fit here the SO mass function by employing a quadratic relation describing the filtered power spectrum shape

$$\ln\sigma^{-1}(M) = -\ln\sigma_{15} + a\ln M + b(\ln M)^2\ , \qquad (8)$$

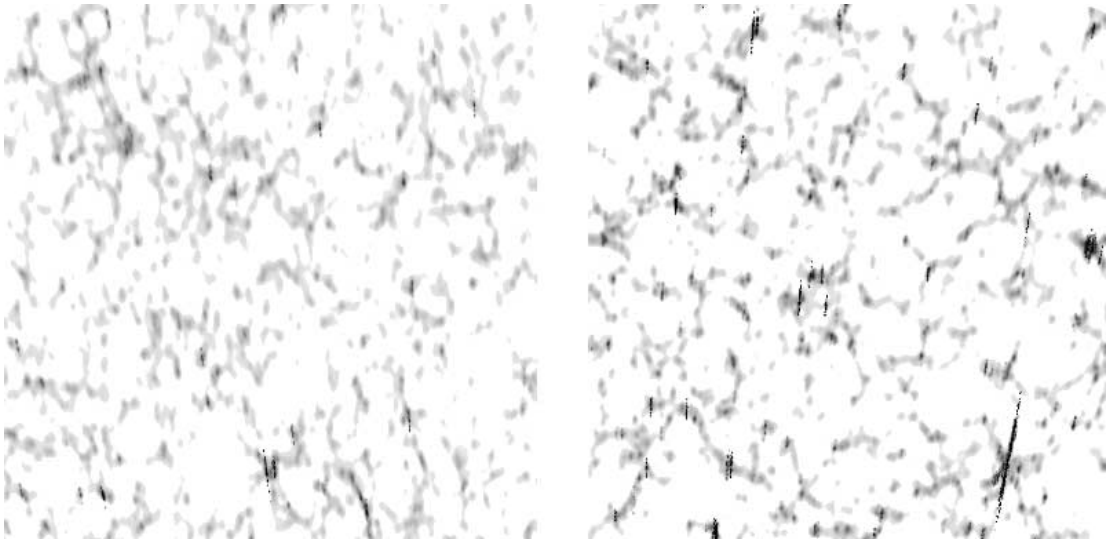

FIG. 4.—Redshift space structure in 75,000 km s^{-1} wide regions centered at $z = 1.1$ in τCDM (*left*) and ΛCDM (*right*). The gray scale shows only overdense material $\delta > 0$. The ΛCDM image includes the most massive cluster in the octant surveys, visible as the long streak at the lower right. The regions shown lie just interior to the vertical edges of the redshift space maps of Fig. 2.

where M is mass in units of $10^{15}\,h^{-1}\,M_\odot$ and the rms fluctuation amplitude σ_{15} at that mass scale is simply related to the fiducial power spectrum normalization by $\ln\sigma_{15} = \ln(\sigma_8) + \text{const}$. Table 3 lists parameters of the fit to equation (8). The maximum error in the fit is 2% in $\ln\sigma^{-1}$ for masses above $10^{13}\,h^{-1}\,M_\odot$. For both models, the effective logarithmic slope,

$$\alpha_{\rm eff}(M) \equiv \frac{d\ln\sigma^{-1}(M)}{d\ln M} = a + 2b\ln M\ , \qquad (9)$$

slowly varies between 0.2 and 0.3 for masses in the range 10^{13}–$10^{15.5}\,h^{-1}\,M_\odot$. The JMF expression for the differential number density as a function of mass and redshift

$$n_{\rm JMF}(M,\,z) = \frac{A\bar{\rho}_m(z)}{M}\alpha_{\rm eff}(M)\exp\left[-\left|\ln\sigma^{-1}(M) + B\right|^{\epsilon}\right] \qquad (10)$$

is the form that we fit to the simulated cluster catalogs.

The critical SO(200) mass functions at $z = 0$ for both models are shown in Figure 5, derived from samples of 1.39 million (ΛCDM) and 1.48 million (τCDM) clusters above $5\times10^{13}\,h^{-1}\,M_\odot$. Fits to equation (10) are shown as dotted lines, with fit parameters listed in Table 4. The upper panels of Figure 5 show the fractional deviations $\delta n/n = n/n_{\rm JMF} - 1$ in bins of width 0.12 in $\ln M$. Error bars assume Poisson statistics. For bins with 100 or more clusters ($M_{200} \lesssim 2\times10^{15}\ h^{-1}\ M_\odot$), the rms deviations $\langle(\delta n/n)^2\rangle^{1/2}$ are $\lesssim 3\%$ (Table 4).

TABLE 3
FIT PARAMETERS FOR $\ln\sigma^{-1}(M)$

Model	σ_{15}	a	b
ΛCDM.....	0.578	0.281	0.0123
τCDM	0.527	0.267	0.0122

NOTE.—See eq. (8).

The high statistical precision of these fits is a lower bound on the absolute accuracy of the mass function calibration. Based on the fits performed by J01 to a large ensemble of simulations covering a wider dynamic range in scale than

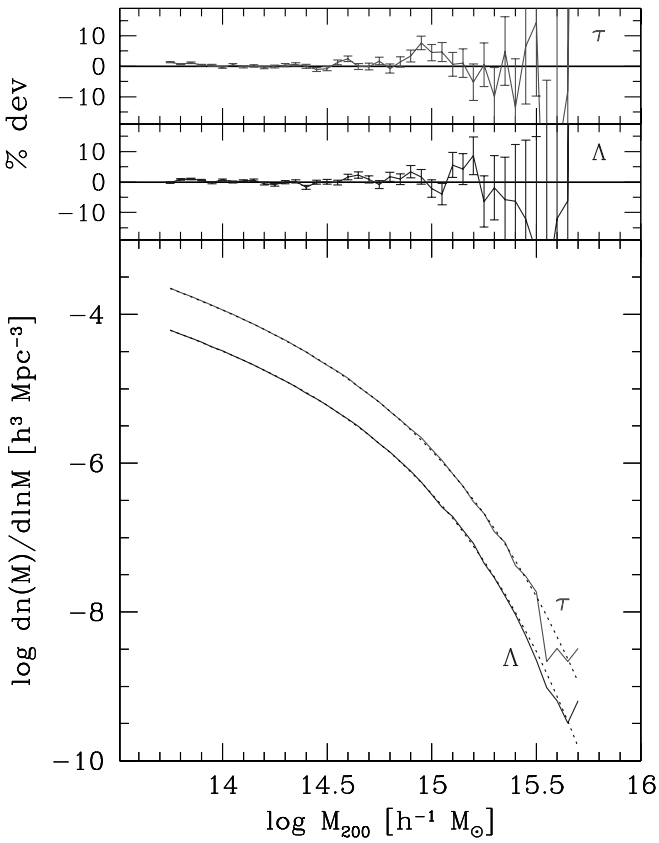

FIG. 5.—*Bottom*: Critical SO(200) mass functions derived from the $z = 0$ HV cluster catalogs (*solid lines*) along with fits to the JMF (eq. [10]) using parameters listed in Table 4 (*dotted lines*). *Top*: Percent deviation in number density between the HV data and the fits. Error bars are based on Poisson statistics in each mass bin. [*See the electronic edition of the Journal for a color version of this figure*.]

TABLE 4
SO(200) Mass Function Parameters

Model	A	B	ϵ	$\langle(\delta n/n)^2\rangle^{1/2}$
ΛCDM.....	0.22	0.73	3.86	0.026
τCDM	0.27	0.65	3.77	0.028

Note.—See eq. (10).

the high-velocity (HV) models alone, we estimate that the normalization A may be systematically low by ~10% (see Appendix A). Considering that this degree of uncertainty in A corresponds to an uncertainty in mass of only 2%–3%, this level of accuracy is sufficient for the practical purpose of comparing to current and near future observations, for which the level of systematic uncertainty in mass is an order of magnitude larger.

Another estimate of systematic error is provided by comparing our results to the recent large simulations of Bode et al. (2001). Their 1 h^{-1} Gpc ΛCDM simulation assumes identical cosmological parameters to our model but uses a particle mass and gravitational softening smaller by factors of 30 and 7. Bode et al. (2001) employ a measure of mass within a comoving radius 1.5 h^{-1} Mpc; this scale encompasses a critical density contrast of 200 at the present epoch for mass $M_{200} = 7.94 \times 10^{14}\ h^{-1}\ M_\odot$. From their Figure 6, the space density of clusters above that mass scale is $10^{-6.6} \sim 2.5 \times 10^{-7}\ h^3\ \mathrm{Mpc}^{-3}$. In our 27 h^{-3} Gpc^3 volume, we find 6499 clusters above this mass limit, implying a space density of $2.4 \times 10^{-7}\ h^3\ \mathrm{Mpc}^{-3}$.

Figure 5 shows that the two models do not produce identical mass functions at the present epoch; the ΛCDM space density is lower by a factor of ~4 than that of τCDM. Two factors combine to make this difference. The first is that our chosen values of σ_8 straddle the constraint derived from fitting the local X-ray cluster space density, such as that quoted in equation (3). The sense of the differences—the ΛCDM model has lower amplitude and τCDM higher, both by about 10%—pushes the models in opposite directions. The second factor is that our choice of fixed critical threshold $\Delta = 200$ leads to smaller masses for ΛCDM clusters. Previous work has typically employed the lower Ω_m-dependent thresholds derived by Eke et al. (1996) from the spherical collapse solutions of Lahav et al. (1991) and Lilje (1992). For $\Omega_m = 0.3$, Eke et al. (1996) calculate critical threshold $\Delta = 97.2$, leading to masses larger by a factor of ~1.25 compared to $\Delta = 200$.

3.4. *Sky Survey Cluster Populations*

We define cluster catalogs in the sky survey output using the same SO algorithm applied to the snapshots at fixed proper time. A minor modification for the ΛCDM model must be made in order to define the threshold Δ with respect to the epoch-dependent critical mass density $\rho_c(z) = \rho_c(0)[\Omega_m(1+z)^3 + \Omega_\Lambda]$.

For the choice $\Delta = 200$, Table 5 lists counts of clusters identified in the sky survey catalogs above mass limits 5×10^{13}, 1×10^{14}, and $1 \times 10^{15}\ h^{-1}\ M_\odot$. The lower mass limit corresponds to 22 particles, and the maximum redshifts of the catalogs are given in Table 2.

Total counts of 1.5 and 0.9 million clusters offer large statistical samples. On the other hand, the small numbers of objects at the most massive end of the spectrum put the finite size of the visible universe into context and provide additional motivation for near-future surveys to define an absolutely complete sample of the largest clusters in the universe. Only a few hundred Coma-like or larger clusters are expected on the sky at all redshifts in either cosmology.

Figure 6 shows redshift space maps of clusters with $M_{200} > 10^{14}\ h^{-1}\ M_\odot$ and $z \le 1.25$ in $3^\circ \times 90^\circ$ strips taken from the PO octant surveys of the τCDM (*left*) and ΛCDM (*right*) models. The surveys display markedly different evolution at $z > 0.5$; distant clusters are more abundant in the low-mass density cosmology (White et al. 1993; Eke et al. 1996; Bahcall et al. 1997). Within the 3° slice—a width equivalent to two SDSS scans—the ΛCDM model contains 3084 clusters above $10^{14}\ h^{-1}\ M_\odot$, half lying beyond $z = 0.70$. The τCDM model contains 1122 clusters, with median $z = 0.39$.

The sky surface density of clusters within three broad redshift intervals is shown as a cumulative function of mass in Figure 7. The ranges in redshift are chosen to represent three classes of observation: local, $z < 0.2$; intermediate, $0.2 \le z < 0.5$; and high, $0.5 \le z < 1.2$. Counts measured within the octant surveys are shown as points, while solid lines show the number expected from integrating the JMF $N(>M) = \int_{z_{\min}}^{z_{\max}} dz (dV/dz) \int_{\ln M}^{\infty} d\ln M' n_{\mathrm{JMF}}(M', z)$.

For τCDM, the integral is performed using the fit parameters determined at $z = 0$ (Table 4). For ΛCDM, we must recognize the fact that, because $\Omega_m(z)$ varies along the light cone, the fit parameters will evolve with redshift. Since Ω_m tends to unity at high redshifts, we expect the parameters to converge to the τCDM values. Since differences in A, B, and ϵ between the two models are small at $z = 0$, we take a simple approach and vary the parameters linearly in Ω_m. For

TABLE 5
Counts of Clusters with $hM_{200}/M_\odot$ above Mass Limits

	ΛCDM			τCDM		
Survey	5×10^{13}	10^{14}	10^{15}	5×10^{13}	10^{14}	10^{15}
MS.....	564875	178223	322	377043	102742	120
VS.....	565886	178483	285	378548	103157	111
PO	255083	64608	45	107900	22853	10
NO.....	259279	64930	42	108807	23216	13
DW.....	5238	1316	1	1833	411	0
Total	1504620	441833	623	878356	226602	231

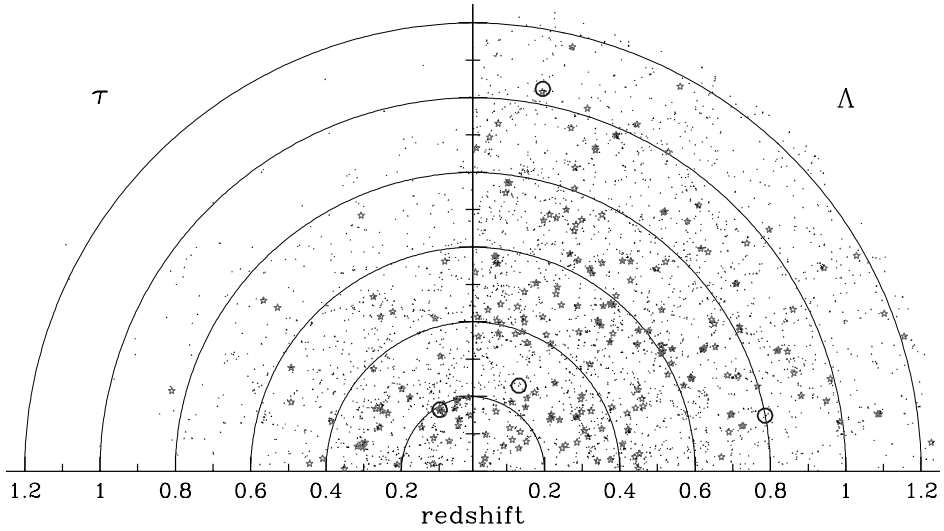

FIG. 6.—Maps of clusters in $90^\circ \times 3^\circ$ slices extending to $z = 1.25$, derived from the octant sky surveys of the τCDM (*left*) and ΛCDM (*right*) models. Symbols shows clusters of different masses: $hM_{200}/M_\odot > 10^{15}$ (*open circles*), $\in 10^{14.5}$–10^{15} (*stars*), and $\in 10^{14}$–$10^{14.5}$ (*dots*). Numbers of clusters in these mass ranges are 1, 50, and 1071 (τCDM) and 3, 185, and 2896 (ΛCDM). [*See the electronic edition of the Journal for a color version of this figure.*]

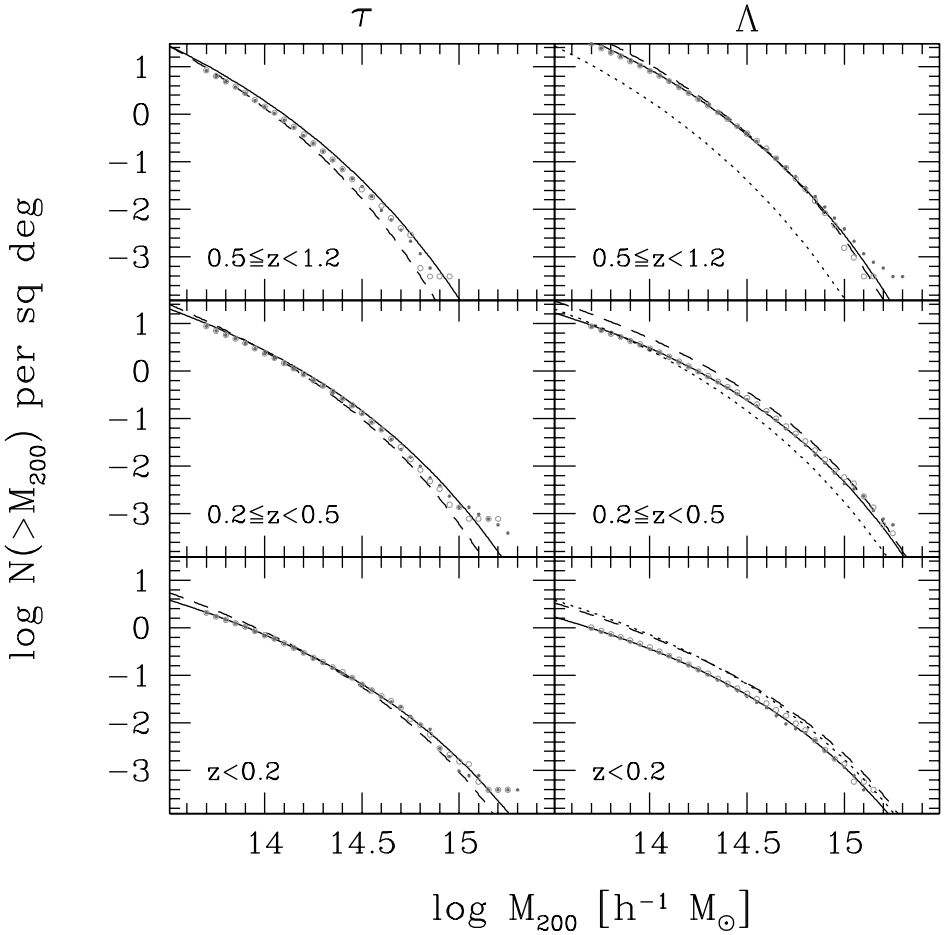

FIG. 7.—Cumulative sky counts of clusters as a function of mass for low-, intermediate-, and high-redshift intervals (*bottom to top*) for τCDM (*left*) and ΛCDM (*right*). The smooth solid lines in each panel give the expectations from integrating the JMF (eq. [10]) over the appropriate volumes. Points show counts from the PO (*filled circles*) and NO (*open circles*) octant surveys. The dashed lines are standard PS estimates. In the ΛCDM panels, the dotted lines display the corresponding JMF expectations for the τCDM cosmology. [*See the electronic edition of the Journal for a color version of this figure.*]

example, we assume for A that

$$A(\Omega_m) = (1 - x)A(1) + xA(0.3) \ , \qquad (11)$$

where $x \equiv (1 - \Omega_m)/0.7$ and $A(1)$ and $A(0.3)$ are the $z = 0$ fit parameters for τCDM and ΛCDM from Table 4. Similar interpolations are assumed for B and ϵ.

The predictions of this model agree very well with the measured counts in the octant surveys. The model is accurate to $\lesssim 10\%$ in number for ΛCDM at all masses and redshifts shown. Similar accuracy is displayed for the τCDM model at low and intermediate redshifts, but the model systematically underestimates counts in the high-redshift interval by $\sim 25\%$.

Dashed lines in Figure 7 show numbers expected by the PS model in its simplest form (see J01 for details). For the τCDM model, the PS curve tends to underestimate the space density at high masses. For the ΛCDM model, the use of mass measured within a critical, rather than mean, mass density threshold leads to an offset in mass between the measured counts and PS curves at low redshifts. The offset declines as Ω_m approaches unity, resulting in a relatively good match to the simulated counts in the high-redshift interval.

In the ΛCDM panels, we plot the τCDM JMF curves as dotted lines for comparison. At low redshifts, the two models exhibit an offset in the direction of τCDM being overabundant relative to ΛCDM, a difference already discussed in § 3.3 for the $z = 0$ population. In the intermediate-redshift interval, this offset is reversed at nearly all masses above the $5 \times 10^{13}\ h^{-1}\ M_\odot$ limit. At high redshifts, the ΛCDM counts are typically an order of magnitude higher than those of τCDM.

3.5. *Sky Survey Completeness*

Comparison of the octant counts with the JMF expectations provides a measure of the incompleteness of the HV sky catalogs that arises from their finite-redshift extent.

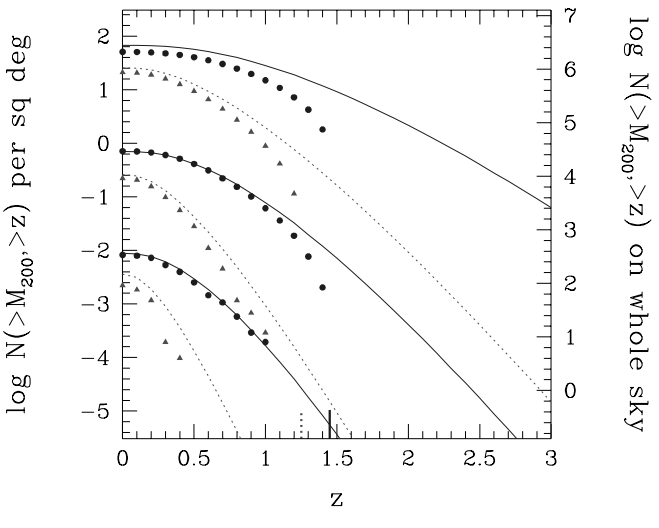

FIG. 8.—Sky surface density of clusters lying at redshift z or higher in ΛCDM (*filled circles, solid lines*) and τCDM (*filled triangles, dotted lines*). Points give numbers derived from the combined octant surveys with masses above $M_{200} = 5 \times 10^{13}$ (*top*), 3×10^{14} (*middle*), and $10^{15}\ h^{-1}\ M_\odot$ (*bottom*). The short vertical lines mark the limiting redshifts of the octant surveys. Lines are expectations at each mass limit derived from integrating the JMF. [*See the electronic edition of the Journal for a color version of this figure.*]

Figure 8 plots the cumulative sky surface density of clusters above mass limits 5×10^{13}, 3×10^{14}, and $10^{15}\ h^{-1}\ M_\odot$ as a function of redshift. Points show the sky densities of clusters lying at redshift z or higher with masses above the stated limits (top to bottom, respectively), determined by combining the octant surveys of each model. Lines in the figure show the JMF expectations from integrating equation (10) using the linear evolution of the fit parameters (eq. [11]).

At Coma mass scales ($>10^{15}\ h^{-1}\ M_\odot$), the catalogs are essentially complete since fewer than one such object is expected over π steradian beyond the survey redshift limit. At $3 \times 10^{14}\ h^{-1}\ M_\odot$, the ΛCDM model octants are missing ~ 100 clusters expected above $z = 1.5$, implying $\sim 98\%$ completeness. The τCDM model at this mass limit is essentially complete; the small discrepancy between the measured and JMF counts at redshifts $z \gtrsim 0.5$ reflects the systematic trend exhibited in the high-redshift panel of Figure 7. At the mass scale of groups, $5 \times 10^{13}\ h^{-1}\ M_\odot$, the incompleteness becomes more significant. In the ΛCDM model, for example, $\sim 15\%$ of the group population should lie at $z > 1.5$.

The ΛCDM model possesses a healthy population of very high redshift clusters. Across the whole sky, a cluster as massive as Coma is expected at redshifts as high as 1.3. At $z > 2.5$, one $3 \times 10^{14}\ h^{-1}\ M_\odot$ cluster should lie somewhere on the sky, joined by $\sim 20{,}000$ others above $5 \times 10^{13}\ h^{-1}\ M_\odot$, nearly 1 cluster deg^{-2}. Before getting carried away by such seemingly firm predictions, we must investigate the effect of varying a degree of freedom that has so far been kept fixed in the models: the amplitude of the fluctuation power spectrum σ_8.

4. THE TEMPERATURE FUNCTION, ABSOLUTE MASS SCALE, AND POWER SPECTRUM NORMALIZATION UNCERTAINTY

In this section we use the freedom in the mass-temperature relation to tune β, the ratio of specific energies in dark matter and ICM gas, so that both models match the observed local temperature function. We show how β should scale with σ_8 so as to maintain consistency with observations. The final snapshots are used to calibrate the level of uncertainty in σ_8 arising from sample variance in local volumes. We discuss the overall systematic error in σ_8 and then examine in § 5 how this uncertainty affects predictions for the high-redshift cluster population.

4.1. *Fitting Local Temperature Observations*

PSW provide the most recent study of the local temperature function and its constraints on σ_8. The sample of 38 clusters used in their analysis is adapted from the X-ray flux-limited sample of Markevitch (1998) and is designed as an essentially volume-limited sample within redshifts $0.03 < z < 0.09$ and Galactic latitude $|b| > 20°$ for clusters with $kT \gtrsim 6$ keV. PSW update temperatures for 23 clusters in the Markevitch (1998) sample with values given in White (2000).

PSW note that the White temperature values, derived from *ASCA* observations using a multiphase model of cluster cooling flow emission, tend to be hotter (by 14% on average) than those Markevitch obtained through a single-temperature fit after exclusion of a core emission. Based on recent high-resolution studies of cooling flows (David et al. 2001; McNamara 2001) that do not appear to support the

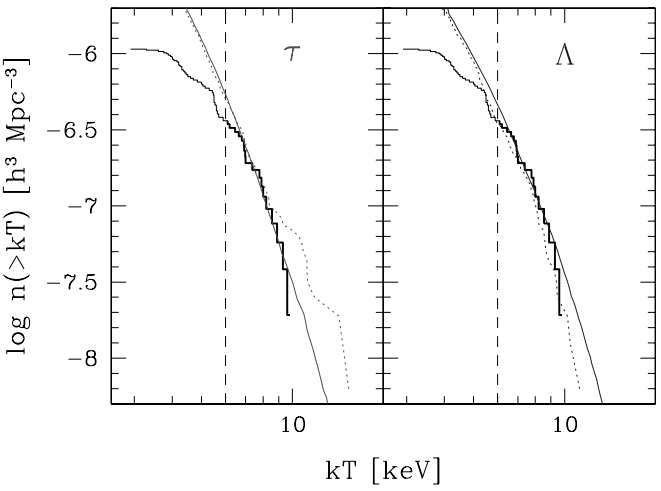

FIG. 9.—Local temperature function of PSW (*thick lines*) based largely on data of Markevitch (1998). The HV simulation expectations, using best-fit values $\beta_\Lambda = 0.92$ and $\beta_\tau = 1.20$, are shown from the light cone (*dotted lines*) and $z = 0$ snapshot (*solid lines*) outputs. The former uses clusters within the combined MS and VS surveys lying in the redshift interval $0.03 < z < 0.09$. The latter uses the cluster population of the entire computational volume. The vertical dashed line in each panel shows the approximate completeness limit of the observations. [*See the electronic edition of the Journal for a color version of this figure.*]

underlying cooling flow emission model used by White (2000), there is cause for concern that the increased temperatures may be artificial. We therefore revert to the original values of Markevitch (1998) and note that the resulting effect on the derived values of β is about 10%.

We use the data from Tables 3 and 4 of PSW and perform a maximum likelihood fit to determine values of β for each model. Our procedure is similar to that used by PSW,[12] but rather than use an analytic model as a reference, we use the binned $z = 0$ differential velocity distribution $n(\sigma_v)$ converted to a set of temperature functions $n(T)$ for β in the range 0.2–2. For a given β, 300 Monte Carlo realizations of the observational sample are generated, assuming Gaussian statistics and temperature errors distributed evenly in number (half positive, half negative) about the best-fit value. To consider those clusters for which the selection volume is best defined and for which cluster ICM physics is better understood, a lower limit of 6 keV is applied to each random realization.

Figure 9 shows a cumulative number of clusters as a function of temperature. The thick line in each panel gives the observations, while the thin solid line shows the $z = 0$ snapshot number density obtained using best-fit values $\beta_\Lambda = 0.92$ and $\beta_\tau = 1.20$. The dotted line shows sky survey results for clusters lying within the range observed, $0.03 < z < 0.09$, using combined MS and VS samples and values $\beta_\Lambda = 0.92$ and $\beta_\tau = 1.10$.

The fact that a single value of β_Λ leads to acceptable fits for both the snapshot and sky survey samples indicates that number evolution in the sky survey sample is small for ΛCDM. The evolution in the τCDM case is sufficient to warrant a slightly lower value of β_τ for the sky survey data. The likelihood analysis described above produces 1 σ error estimates $\beta_\Lambda = 0.92 \pm 0.06$ and $\beta_\tau = 1.10 \pm 0.06$. Current samples constrain the temperature scale of the cluster population to an accuracy of about 6%.

[12] We note a typographical error in their eq. (18), which should read $\ln \mathscr{L} = \sum_i \{(\eta_i - 1)\mu_i + \eta_i \ln[1 - \exp(-\mu_i)]\}$.

4.2. *Cosmic Variance Uncertainty in σ_8*

The locally observed cluster sample is one realization of a cosmic ensemble that varies because of shot noise and spatial clustering on survey scales. Except for extending the angular coverage of the observations into the plane of the galaxy, there is no possibility of observing another cluster sample in the same redshift range. Cosmic variance in the local sample can be investigated using the large sampling volumes of the simulations.

An impression of the magnitude of the sample variation is given in Figure 10. Differential mass functions for 16 independent 5000 deg^2 survey volumes, extending to $z = 0.15$ and extracted from the MS and VS samples, are shown for the ΛCDM model. A mass limit of $5 \times 10^{14}\ h^{-1}\ M_\odot$ leads to an average sample size of 30 clusters. Dotted lines in each panel show the range in number density of the ΛCDM JMF as σ_8 is raised and lowered by 5% about its default. The sky survey sample variations are largely confined within the ±5% range of σ_8 shown.

The full $z = 0$ snapshot samples allow a more precise estimate of the cosmic variance contribution to σ_8 error. We divide the full computational volumes into cubic cells of size 375 (ΛCDM) and 400 h^{-1} Mpc (τCDM). Offsetting the grid of cells by a half-cell width along the principal axes and resampling generates totals of 4096 and 1000 samples of clusters in cells of volume comparable to the 5×10^7 (h^{-1} Mpc)^3 sampled by local temperature observations. Within each cell, we determine the most likely value of σ_8 using the JMF space density fit to mass-limited samples. Mass limits of 6×10^{14} (ΛCDM) and $10^{15}\ h^{-1}\ M_\odot$ (τCDM) produce average counts of 30 clusters within each cell.

The distributions of σ_8 resulting from this exercise are nearly lognormal; we find $\sigma_8 = 0.911e^{\pm 0.030}$ and $0.591e^{\pm 0.023}$ for ΛCDM and τCDM, respectively.

The error in σ_8 from the likelihood analysis is well approximated by

$$\frac{\Delta\sigma_8}{\sigma_8} = \frac{\langle (N - \bar{N})^2 \rangle^{1/2}}{\bar{N}} \left| \frac{\sigma_8}{n(M)} \frac{\partial n(M)}{\partial \sigma_8} \right|^{-1}_{M_{\rm lim}}, \qquad (12)$$

where $\langle (N - \bar{N})^2 \rangle^{1/2}$ is the rms deviation of counts in cells above the mass limit, $\bar{N}$ is the mean count, and the Jacobian is evaluated at the survey mass limit $M_{\rm lim}$. The latter is a steep function of mass, taking on values 5.8 and 8.3 for ΛCDM and τCDM, respectively.

Because of scatter in the temperature-mass relation, the variance of counts in cells for temperature-limited samples is slightly larger than that of mass-limited samples. Performing a similar analysis based on counts for temperature-limited samples results in $\Delta\sigma_8/\sigma_8 = 0.039$ for ΛCDM and 0.025 for τCDM. Since observations are temperature-limited, these values apply to analysis of current temperature data.

4.3. *M-T Calibration and Overall σ_8 Uncertainty*

As emphasized by previous studies, uncertainty in the calibration of $p(M|T)$ is the largest source of error in σ_8. The error in σ_8 associated with uncertainty in the absolute mass scale can be derived by solving for the zero in the total deriv-

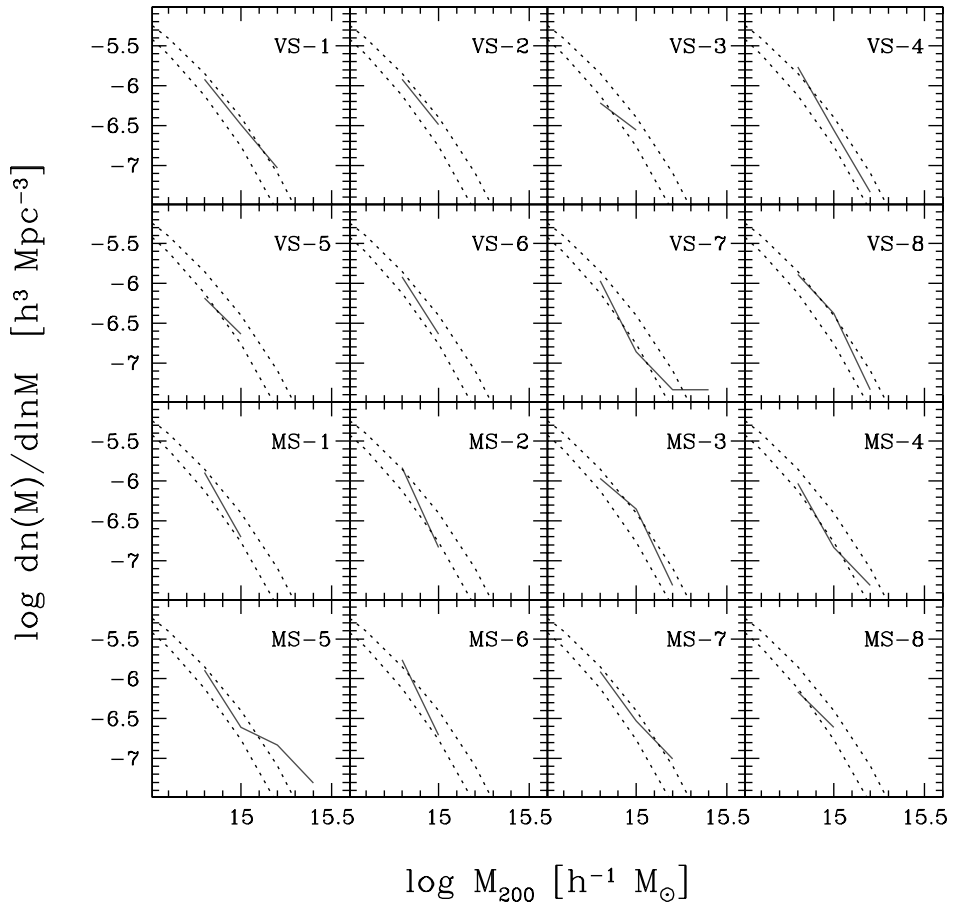

FIG. 10.—Differential mass functions within 16 independent $\pi/2$ steradian regions extending to $z = 0.15$, derived from the MS and VS surveys of the ΛCDM el. The dashed lines show JMF expectations (eq. [10]) for σ_8 values varied by ±5% about the input value linearly evolved to $z = 0.1$. The volume of the samples is comparable to that of the local observed sample used to constrain σ_8. [*See the electronic edition of the Journal for a color version of this figure.*]

ative of the mass function (eq. [10]). Ignoring the weak mass dependence of $\alpha_{\rm eff}(M)$, the result is

$$\frac{\Delta\sigma_8}{\sigma_8} = \alpha'(M)\frac{\Delta M}{M} \ , \qquad (13)$$

where, at large masses $[\sigma(M) < e^B]$,

$$\alpha'(M) = \alpha_{\rm eff}(M) + \frac{1}{\epsilon[\ln\sigma^{-1}(M) + B]^{\epsilon-1}} \ . \qquad (14)$$

The first term can be connected to a shift in the characteristic collapsed mass (fixed e^B), while the second term, which arises from the $1/M$ factor in equation (10), is required to maintain constant mass fraction in objects at fixed $\ln\sigma^{-1}(M)$. The sensitivity $\alpha'(M)$, plotted in Figure 11, asymptotes to a value 0.4 above $\sim 5 \times 10^{14}\ h^{-1}\ M_\odot$ in both cosmologies. Below this mass, $\alpha'(M)$ increases considerably, reaching unity at $10^{14}\ h^{-1}\ M_\odot$. The rarest, most massive clusters place the most sensitive limits on σ_8.

Attempts at calibrating the mass-temperature relation have been made using numerical simulations and observations. Simulation results by different groups compiled by Henry (2000) and PSW display an overall range of ∼50% in temperature at fixed mass, equivalent to a 75% range in mass if one assumes $M \propto T^{3/2}$. A complicating factor is that normalizations are typically quoted using a mass-weighted temperature, and this measure can differ systematically at

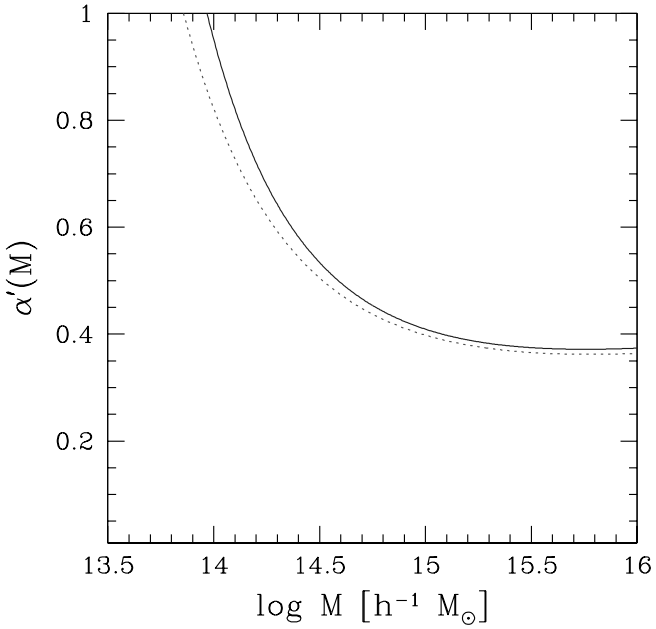

FIG. 11.—Sensitivity $\alpha'(M)$ (eq. [14]) for the ΛCDM (*solid line*) and τCDM (*dotted line*) models. [*See the electronic edition of the Journal for a color version of this figure.*]

the ~20% level from the spectral temperatures derived from plasma emission modeling of the simulated ICM (Mathiesen & Evrard 2001). Observational attempts at calibrating the relation (Horner et al. 1999; Nevalainen et al. 2000; Finoguenov, Reiprich, & Böhringer 2001) display discrepancies of similar magnitude to the simulations. Part of this variation is due to the fact that these analyses are comparing T to estimators $\hat{M}$ that differ in their degree of bias and noise with respect to the theoretical mass M_Δ.

With relatively little in the way of firm justification, we conservatively estimate the 1 σ uncertainty in the zero point of the mass-temperature relation to be $\Delta M/M = 0.25$. Assuming lognormal errors, this assumption allows the absolute mass scale to lie within a factor of 2.3 range at 90% confidence. We note that PSW assume a 15% uncertainty in mass, somewhat smaller than the value used here.

From equation (13) in the high-mass limit, the uncertainty in power spectrum normalization is

$$\left|\frac{\Delta\sigma_8}{\sigma_8}\right|_{\rm sys} = 0.10\ (1\ \sigma)\ , \tag{15}$$

or a 16% uncertainty at 90% confidence. We employ this level of error when exploring statistics of high-redshift clusters in § 5.

4.4. *Degeneracy in β and σ_8*

The calibration uncertainty discussed above in terms of mass can be rephrased in terms of temperature or, equivalently for this study, the parameter β used to connect temperature to dark matter velocity dispersion. An advantage of β is that it can be determined independently from gasdynamic simulations that model the gravitationally coupled evolution of the ICM and dark matter. In a comparison study of 12 largely independent simulation codes applied to the formation of a single cluster, Frenk et al. (1999) find good agreement among the computed specific energy ratios within $\Delta = 200$, with mean and standard deviation $\beta_{\rm sim} = 1.17 \pm 0.05$.

At first glance, this determination agrees well with the τCDM value of β but is in mild (2.7 σ) disagreement with the ΛCDM value derived from the local temperature sample in § 4.1. However, the uncertainties quoted previously for β are derived at the fixed values of σ_8 used in the N-body simulations. To incorporate the additional sources of error in σ_8 discussed above, we use the mass sensitivity, equation (13) and the virial scaling $T \propto \beta^{-1} M^p$ with $p \simeq \frac{2}{3}$ exhibited by gasdynamic simulations of clusters to derive the scaling:

$$\beta \propto \sigma_8^{p/\alpha'(M)} \sim \sigma_8^{5/3}\ . \tag{16}$$

An increase in β_Λ sufficient to match the Frenk et al. (1999) simulation ensemble value requires $\sigma_8 = 1.04$. This value is marginally within the range allowed by *COBE* microwave background anisotropy constraints for the Hubble parameter $h \sim 0.7$ (Eke et al. 1996). Tighter constraints on σ_8 could serve to increase the tension between the two independent determinations of the specific energy ratio.

5. CLUSTERS AT HIGH REDSHIFT

We are now in a position to revisit the expected numbers of high-redshift clusters, incorporating into the analysis the systematic uncertainty in power spectrum normalization. We begin by noting the advantage of predicting cluster counts as a function of X-ray temperature rather than mass and compare the model predictions to the sky surface density of high-redshift clusters from the Extended Medium-Sensitivity Survey (EMSS) catalog (Henry et al. 1992; Gioia & Luppino 1994). Redshift information from the *ROSAT* Deep Cluster Survey (RDCS) catalog (Rosati et al. 1998; Borgani et al. 1999b) supports the ΛCDM model under conservative assumptions, but the model predictions are sensitive to selection effects related to core luminosity evolution.

We then return to mass-selected samples and explore the sensitivity of SZ searches for distant clusters to σ_8 variation. Finally, the redshift evolution of characteristic mass and temperature scales at fixed sky surface density is used to compare ΛCDM and τCDM expectations against redshift and temperature extremes of the observed cluster population.

5.1. *X-Ray Cluster Counts*

Because models are constrained by observations of the local temperature function, predictions of counts as a function of temperature can be made with smaller uncertainty than predictions of counts as a function of mass. The mass function requires separate knowledge of β and σ_8, whereas the temperature function requires only a unique combination of the pair. This advantage breaks down if β (or an equivalent parameter linking T to M) evolves with redshift. Current observations support no evolution (Tran et al. 1999; Wu et al. 1999), at least for the connection between galaxy velocity dispersion and ICM temperature. We therefore assume a nonevolving β in order to examine the space density of clusters as a function of temperature at arbitrary redshift.

Figure 12 shows the range of cumulative sky counts expected as a function of temperature within the same three broad redshift intervals used in Figure 7. The range in counts shown within each panel corresponds to varying $\ln\beta$ within its 90% confidence region with σ_8 held fixed for each model: $0.83 \le \beta_\Lambda \le 1.01$ and $0.91 \le \beta_\tau \le 1.20$. The constraint to match local observations produces nearly complete overlap in the temperature functions of the two cosmologies at $z < 0.2$. At intermediate redshifts, the ΛCDM counts are boosted by nearly an order of magnitude compared to the low-redshift range, while the τCDM counts grow by a factor of ~3. The 90% confidence regions for the models become disjointed in this redshift interval.

In the high-redshift region, the models separate further, with the characteristic temperature at fixed sky surface density a factor of ~1.5 times larger in ΛCDM than τCDM. The steep nature of the space density translates this moderate difference in T into a large factor difference in counts; at 8 keV, the counts differ by a factor of about 20. An estimate of the observed sky density in this redshift range, based on the EMSS data, is shown as the square in the upper panel of Figure 12. This point is based on three hot ($kT > 8$ keV) and distant ($z > 0.5$) clusters covering a search area of 278 deg^2 (Henry 2000), leading to a sky surface density 0.011 deg^{-2} at $z > 0.5$. The data are consistent with the ΛCDM expectations and rule out τCDM at more than 99% confidence.

A modest degree of evolution in β_τ with redshift could reconcile τCDM with the EMSS data. Additional information, such as the redshift distribution of X-ray flux-limited

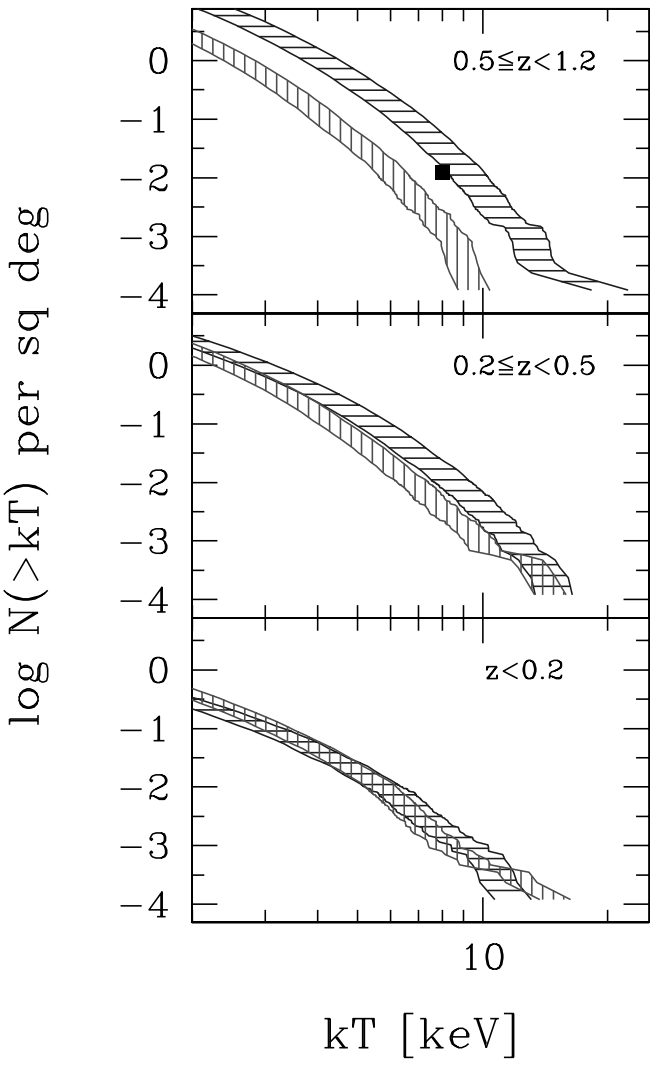

FIG. 12.—Range of cumulative sky surface densities of clusters as a function of temperature in three redshift intervals for the ΛCDM (*horizontal hatched regions*) and τCDM (*vertical hatched regions*) cosmologies. The range is determined from the combined octant survey counts by varying β within its overall 5% to 95% confidence range. The filled square denotes the EMSS observational result for clusters hotter than 8 keV at $z > 0.5$. [*See the electronic edition of the Journal for a color version of this figure*.]

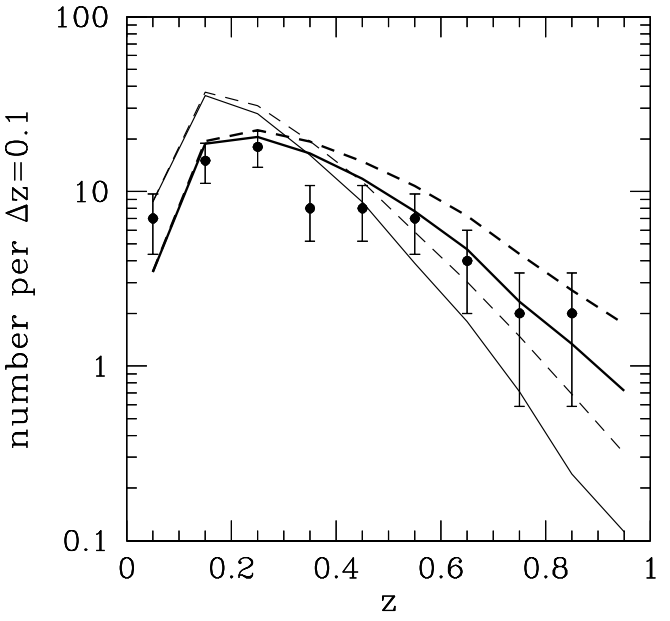

FIG. 13.—Points show the redshift distribution of the X-ray flux-limited RDCS (Rosati et al. 1998; Borgani et al. 1999b) with Poissonian errors. The solid lines show expectations for a 33 deg^2 survey derived from the combined octant surveys by assuming constant β and a nonevolving L_X-T relation. The thick lines are ΛCDM predictions; the thin lines are τCDM. The dashed lines show plausible confusion effects of core luminosity contamination on the X-ray selection (see text for details). [*See the electronic edition of the Journal for a color version of this figure*.]

samples, provides independent constraints capable of eliminating such a possibility (Oukbir & Blanchard 1992). The RDCS (Rosati et al. 1998) is currently the X-ray–selected survey with the most extensive redshift data available for distant clusters. The survey, as analyzed by Borgani et al. (1999b), is complete within 33 deg^2 to limiting 0.5–2 keV X-ray flux 5×10^{-14} ergs s^{-1} cm^{-2} and contains 70 clusters with measured redshifts extending to near 1.

To explore the compatibility of the octant survey populations with the RDCS sample requires a model for the X-ray luminosity L_X anticipated from the simulated clusters. As a base model, we assume a mean bolometric L_X-T relation $L_X = 2.9 \times 10^{44}(T/6\ \mathrm{keV})^{2.88}\ h^{-2}$ ergs s^{-1} (Arnaud & Evrard 1999) that is assumed not to evolve with redshift (Mushotzky & Scharf 1997; Henry 2000; Fairley et al. 2000). To account for the fact that the L_X-T mapping is not one-to-one, we add a uniformly distributed scatter of ± 0.4 in $\log_{10}(L_X)$. Fluxes in an observed 0.5–2 keV X-ray band are derived from a MEKAL spectral synthesis code assuming 0.3 solar metallicity. Applying a 5×10^{-14} ergs s^{-1} cm^{-2} flux cut, excluding $z < 0.05$ clusters, and scaling the PO and NO simulated cluster surveys to 33 deg^2 area leads to predictions shown as the solid lines in Figure 13. Under these economical assumptions of ICM evolution, the ΛCDM model provides an acceptable fit to the observations.

Since the most distant cluster sources are typically detected at a modest signal-to-noise ratio, it is worth investigating the influence that additional sources of X-ray emission would have on survey selection. The steep nature of the mass function offers the opportunity for clusters lying just below the survey flux limit to be pushed above it, given some mechanism to enhance its X-ray luminosity.

For the purpose of illustration, we consider adding to the base model described above random additional sources of X-ray luminosity whose influence increases with redshift. These sources may be thought of as arising from cooling flows, active galaxies embedded within or near the cluster, or mergers, any or all of which may be more likely to occur at higher redshift. The specific model assumes that half of the population has luminosities boosted by an amount drawn from a uniform distribution of amplitude $\alpha(z)L_X$, with $\alpha(z) = 2z$ and L_X the base luminosity. Although arguably extreme, this model raises the zero point of the L_X-T relation by only 50% at $z = 0.5$. Expectations for RDCS based on this alternative, shown as dashed lines in Figure 13, differ significantly from the base model predictions at high redshift. The τCDM still fails to match the observations at redshifts between 0.1 and 0.3, but its high-redshift behavior is much improved. The ΛCDM model consistently overpredicts the counts beyond $z = 0.4$.

Deep X-ray imaging with *Chandra* and *XMM* will help settle the issue of whether this toy model is too extreme. For now, we note that the good agreement between the RDCS and the economical ΛCDM model predictions may signal that the ICM undergoes relatively simple evolution dominated by gravitational shock heating after an initial, early epoch of preheating (Evrard & Henry 1991; Kaiser 1991; Bower 1997; Cavaliere, Menzi, & Tozzi 1999; Balogh, Babul, & Patton 1999; Llyod-Davies, Ponman, & Cannon 2000; Bower et al. 2001; Bialek, Evrard, & Mohr 2001; Tozzi & Norman 2001). The preheated cluster simulations of Bialek et al. (2001) produce low-redshift scaling relations for X-ray luminosity, isophotal size, and ICM mass versus temperature that simultaneously match local observations and exhibit little evolution in the L_X-T relation to $z \sim 1$.

5.2. *Mass-selected Samples*

Interferometric SZ surveys have been proposed that would survey $\sim$10 deg^2 of sky per year with sufficient sensitivity to detect all clusters above a total mass limit $\sim 10^{14}\, h^{-1}\, M_\odot$, nearly independent of redshift (Holder et al. 2000; Kneissl et al. 2001). The mass limit assumes that the ICM mass fraction does not depend strongly on cluster mass or redshift, an assumption supported by simulations. Bialek et al. (2001) find that the ICM gas fraction within $\Delta = 200$ remains a fair representation of the baryon-to-total cosmic ratio: $f_{\rm ICM} = (0.92 \pm 0.04)\Omega_b/\Omega_m$ above rest-frame temperature $kT = 4$ keV. We investigate expectations for SZ surveys assuming that they will be sensitive to a limiting total mass that is independent of redshift.

Maps of mass-limited cluster samples in SDSS-like survey slices were presented in Figure 6 for the default values of σ_8. To illustrate the effect of σ_8 variation, we plot clusters in the same spatial regions again in Figure 14, after applying an effective fractional variation in σ_8 of 10% (τCDM) and -10% (ΛCDM). Although equation (13) suggests a simple shift in mass threshold to mimic a change in σ_8, the mass dependence of $\alpha'(M)$ (Fig. 11) introduces cumbersome nonlinearity into the shift. We adopt instead an equivalent procedure that adjusts both masses M and number densities $n(M)$ in the HV cluster catalogs by amounts

$$M' = e^{\mu} M,$$
$$n(M')d\ln M' = e^{-\mu} n(M) d\ln M\ , \qquad (17)$$

with

$$\mu = \frac{\ln(1 + \Delta\sigma_8/\sigma_8)}{\langle \alpha_{\rm eff} \rangle} \qquad (18)$$

and $\langle \alpha_{\rm eff} \rangle = 0.25$. Tests of these transformations using the JMF verify their accuracy to better than 10% in number for masses $10^{13.7}$–$10^{15.3}\ h^{-1}\ M_\odot$ and variations of power spectrum normalization within the 90% confidence region $|\Delta\sigma_8/\sigma_8| \leq 0.16$. The practical value of these simple transformations is in allowing the discrete simulation output to represent a family of models covering a range of normalizations σ_8.

When compared to Figure 6, the intermediate-redshift cluster populations of the two cosmologies shown in Figure 14 appear much more similar. Unlike Figure 6, the overall counts above $10^{14}\, h^{-1}\, M_\odot$ in the 3° slice are now nearly identical—1696 for τCDM compared to 1843 for ΛCDM. However, their redshift distributions remain different; the τCDM clusters stay concentrated at lower redshifts, while the ΛCDM clusters are more broadly distributed (Oukbir & Blanchard 1992).

Figures 6 and 14 imply that a redshift statistic, such as the sample median, will be superior to counts as a means to constrain cosmology. Motivated by the aforementioned planned SZ surveys, we perform a specific investigation of expectations for a random 10 deg^2 survey complete above a mass limit $M_{200} = 10^{14}\, h^{-1}\, M_\odot$. We sample clusters in 3000 randomly located, square fields of 10 deg^2 area, divided equally between the PO and NO surveys and chosen to avoid survey boundaries. We use the transformations in equation (17) to define the cluster population at values of σ_8 different from the default. To drive the models in directions that minimize their differences, we increase σ_8 in the τCDM model and decrease it in the ΛCDM case.

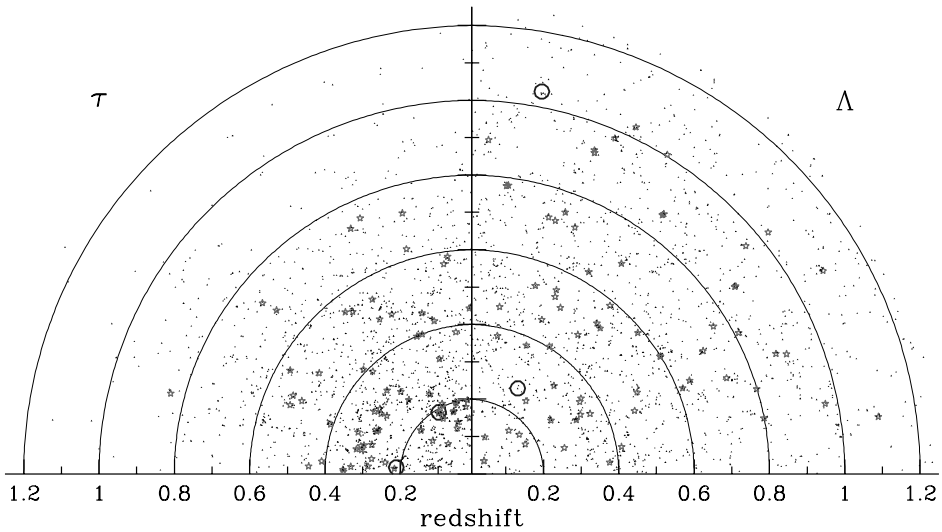

FIG. 14.—Clusters expected in the same 90° × 3° slices shown in Fig. 6, but shown here after application of effective biases in σ_8 of 10% (τCDM) and -10% (ΛCDM). [*See the electronic edition of the Journal for a color version of this figure.*]

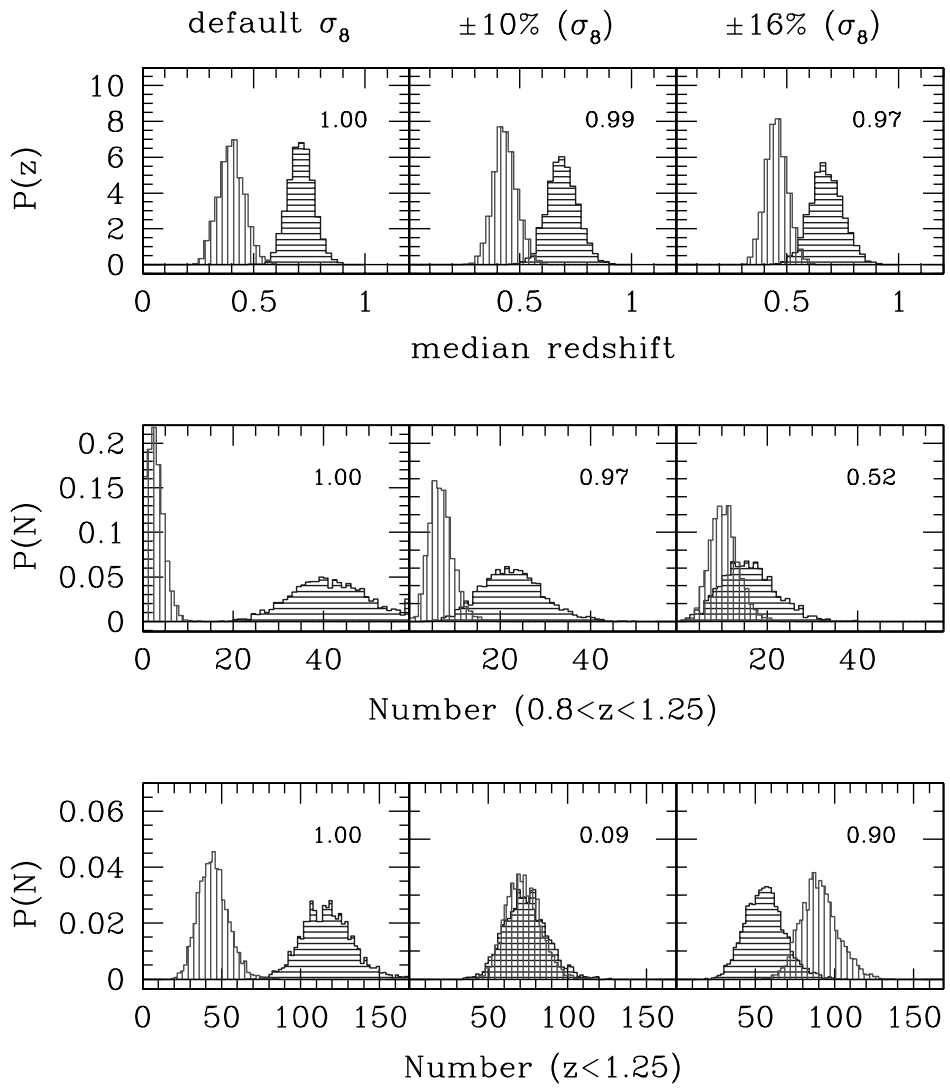

FIG. 15.—Influence of varying σ_8 on the population of clusters more massive than $10^{14}\,h^{-1}\,M_\odot$ expected in 10 deg^2 survey fields. The columns (*left to right*) show probability distributions at the default σ_8 values, ±10% and ±16% variation (positive for τCDM; negative for ΛCDM) for the counts at redshifts $z < 1.25$ (*bottom row*), counts in the high-redshift interval $0.8 < z < 1.25$ (*middle row*), and the median cluster redshift (*top row*). The vertical hatched distributions are τCDM, horizontal are ΛCDM. The numbers in each panel give the power statistic described in the text. The distributions are generated by sampling 10 deg^2 fields around 3000 randomly chosen pointings in the combined octant surveys of each model. Shifts in mass and number (eq. [17]) are used to effectively vary σ_8 in the cluster catalogs. [*See the electronic edition of the Journal for a color version of this figure*.]

The distributions of counts at all redshifts ($z < 1.25$), counts at high redshift ($0.8 < z < 1.25$), and the median redshift for clusters above the survey mass limit derived from the random samples are presented in Figure 15. At the default values of σ_8 (*left-hand column*), the distributions of number expected at either all redshifts $z < 1.25$ (*bottom row*) or high redshift (*middle row*) would allow unambiguous discrimination between the models using a single 10 deg^2 field. At high redshift, the ΛCDM model predicts, on average, a factor of 15 more clusters than τCDM. Overall, the mean counts in 10 deg^2 are 117 and 45, respectively. Biasing σ_8 by 10% in the chosen directions (*middle column*) produces essentially identical expectations for the overall cluster yield, with both models expecting 72 ± 12 clusters per field. At high redshift, the ability to discriminate is weakened. For a 16% bias (*right-hand column*), the sense of the overall counts are reversed, with the τCDM model having a 60% larger yield, on average, than ΛCDM. The high-redshift count distributions of the models possess considerable overlap.

In contrast to the count behavior, the distributions of sample median redshift $z_{\rm med}$ are extremely stable to variations in σ_8. The 95th percentile value of $z_{\rm med}$ for τCDM moves from 0.498 to 0.528 to 0.538 at 0%, 10%, and 16% bias, respectively. As a frequentist measure of discrimination we quote the power (Sachs 1982), defined as the probability of rejecting τCDM at the chosen level (95%) of significance given ΛCDM, as the true model. Measuring the power by integrating the ΛCDM distributions of $z_{\rm med}$ above the 95th percentile τCDM value results in values of 99.9%, 98.8%, and 94.8%. These values measures, and others calculated in a similar manner for the counts, are listed in corresponding panels of Figure 15. High-redshift counts lose power to discriminate between the models as the applied bias on σ_8 is increased.

The large shift in the expected counts as σ_8 is varied provides an appropriate lever arm to use for placing firmer constraints on this parameter with SZ surveys. Holder, Haiman, & Mohr (2001) estimate that a 10 deg^2 survey as assumed here could, with complete redshift information and assuming complete knowledge of the relation between SZ signal and cluster mass, constrain σ_8 at the 3%–5% level.

5.3. *Sky Surface Density of Distant Clusters*

Chandra X-Ray Observatory detections of extended X-ray emission from three clusters at $z > 1$ have recently been reported. Stanford et al. (2001) report detection of hot ICM in a pair of RDCS-selected clusters separated by only 4′ on the sky and 0.01 in redshift, RX J0848+4453 at $z = 1.27$ and RX J0849+4452 at $z = 1.26$ (Stanford et al. 1997; Rosati et al. 1998). RX J0848+4453 appears to have a complex morphology and a cool temperature $kT = 1.6^{+0.8}_{-0.6}$ keV, while RX J0849+4452 appears to be a relaxed system with higher temperature $kT = 5.8^{+2.8}_{-1.7}$ keV. In addition to these systems, Fabian et al. (2001) present *Chandra* evidence for extended ICM emission at temperature $kT = 5.0^{+2.6}_{-1.5}$ keV around the radio galaxy 3C 294 at $z = 1.786$. Quoted errors in these temperature estimates are 68% confidence values.

From the temperature-mass relation calibrated by the local temperature function sample in § 4 and assuming a nonevolving β, we can estimate the masses of these clusters. Results for ΛCDM (τCDM) are $4.4(3.9) \times 10^{13}$ and $M_{200} = 3.1(2.7) \times 10^{14}\ h^{-1}\ M_\odot$ for RX J0848+4453 and RX J0849+4452, respectively, and $M_{200} = 1.9(1.6) \times 10^{14}\ h^{-1}\ M_\odot$ for 3C 294. To explore the likelihood of finding such clusters, we employ a statistic that links physical properties to measurable sky surface density.

The statistics we consider are sky surface density characteristic mass and temperature, defined as the mass $M_{N'}(z)$ and temperature $T_{N'}(z)$ at which the differential sky surface density $N'(z) \equiv dN/dz$ of inversely rank-ordered clusters at redshift z takes on fixed values. The mass scale $M_{N'}(z)$ is defined by the relation

$$N'(z) = \frac{1}{\Omega_{\rm surv}} \int_{M_{N'}(z)}^{\infty} d\ln M\, n(M, z) \frac{dV}{dz}\ , \qquad (19)$$

where $\Omega_{\rm surv}$ is the survey sky area. The characteristic temperature is defined in a similar manner. As a practical approximation to the redshift differential, we employ counts in redshift bins of width 0.1 to derive this statistic from the HV sky survey data.

Figure 16 shows the redshift behavior of the sky surface density characteristic (SSDC) mass and temperature for the ΛCDM model. The symbols are values based on the combined octant survey populations. The solid lines are predictions from the JMF, derived by computing equation (19) using equation (10) for $n_{\rm JMF}(M, z)$ and integrating in bins of width 0.1 in redshift. Sky surface density thresholds dN/dz vary by factors of 10 from 0.001 to 10 deg^{-2} per unit redshift, as labeled. The open circles show results for the SSDC at 0.01 deg^{-2} per unit redshift extending to $z \sim 3$ using the $16^\circ \times 76^\circ$ extension to the PO survey. The thick dashed lines in each panel show the limiting resolved mass of $5 \times 10^{13}\ h^{-1}\ M_\odot$ (22 particles) and the corresponding limiting resolved virial temperature. The good agreement between the Jenkins model and the discrete cluster sample measurements is to be expected from the results of Figure 7; the POX extension data verify the utility of the model to $z \sim 3$.

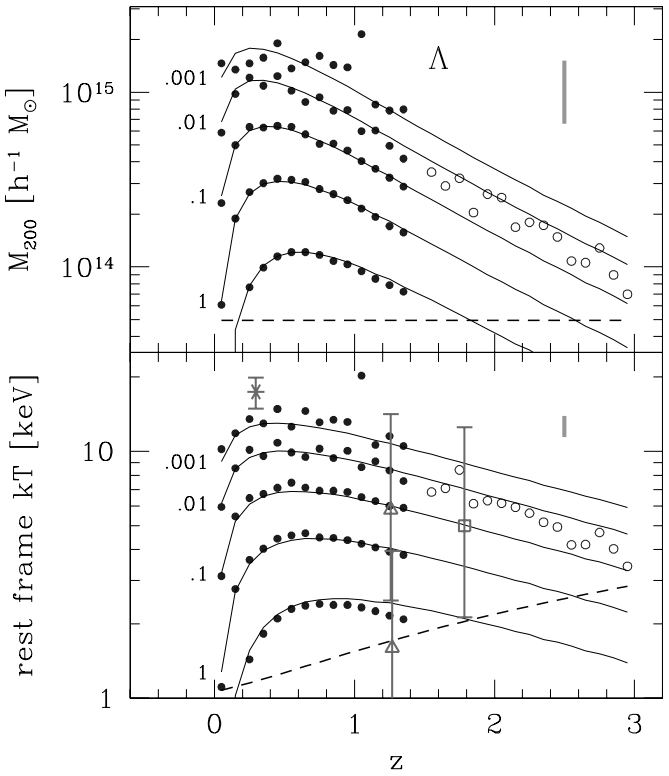

FIG. 16.—Sky surface density characteristic mass (*top*) and temperature (*bottom*) in the ΛCDM model. Points from the 10,000 deg^2 combined octant surveys (*filled circles*) and the 1000 deg^2 extension (*open circles*) show values above which the cluster sky surface density in the redshift interval $z - 0.05$ to $z + 0.05$ exceeds values 0.001, 0.01, 0.1, 1, and 10 deg^{-2} per unit redshift. Clusters at the lowest sky density shown are the most massive or hottest in the particular redshift interval within the combined octants. Note the exceptional "monster" cluster at $z = 1.04$. The solid lines are JMF expectations described in the text. Vertical bars in each panel denote the 90% confidence uncertainty range in the absolute calibration of mass and temperature scales. The open triangles and squares plot extremes of the known X-ray cluster population: RX J0849+4452 at $z = 1.26$ and RX J0848+4453 at $z = 1.27$ (Stanford et al. 2001, *triangles*); 3C 294 at $z = 1.786$ (Fabian et al. 2001, *square*), and 1E 0657−56 at $z = 0.296$ (Tucker et al. 1998, *asterisk*). The dashed lines show a mass limit of 22 simulation particles (*top*) and the virial temperature at that mass (*bottom*). [*See the electronic edition of the Journal for a color version of this figure.*]

The vertical bar in each panel of Figure 16 shows the 90% uncertainty range in the local calibration of each quantity: $e^{\pm 0.11}$ in kT and $e^{\pm 0.42}$ in M. The HV simulation and Jenkins model results for the SSDC measures can be varied vertically by these amounts in Figure 16. The narrow spacings between $M_{N'}(z)$ and $kT_{N'}(z)$ contours reflect the steepness of the cumulative counts at fixed redshift; the terrain of the counts is steep in the mass and temperature directions. At a particular redshift, the calibration uncertainties translate into a large range of allowed sky surface densities for a given mass and a smaller but still significant range for a given temperature.

Although steep in the temperature direction, the contours in the lower panel of Figure 16 are remarkably flat in the redshift direction. Over the entire redshift interval $0.1 < z < 1.5$, the JMF expectations for the SSDC temperature at 0.01 deg^{-2} per unit redshift lie in a narrow range between 8 and 10 keV. In the ΛCDM model, distant, hot clusters should be as abundant on the sky as those nearby.

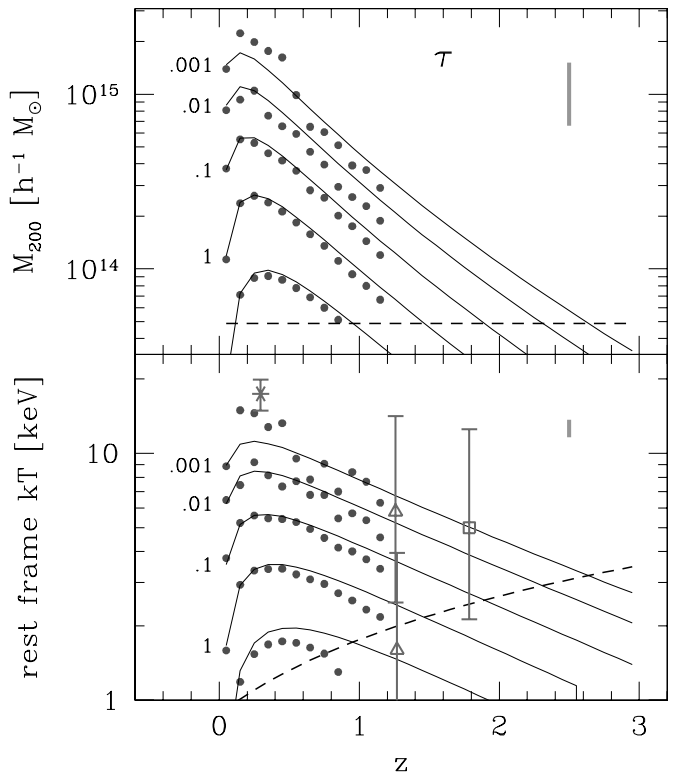

FIG. 17.—Same as Fig. 16, but for the τCDM model. [*See the electronic edition of the Journal for a color version of this figure.*]

Temperatures of the aforementioned observed distant clusters are plotted in the lower panel of Figure 16 as open triangles (the RX clusters) and an open square (3C 294). Temperature uncertainties at 90% confidence are shown, assuming Gaussian statistics to convert 1 σ errors. The central values of the hotter pair are consistent with a sky surface density of 1 cluster 10 deg^{-2} per unit redshift, but within the temperature measurement uncertainties, these objects could be up to a factor of 100 more common or a factor of $\sim$1000 more rare. The lower temperature system at $z = 1.27$ is consistent with a surface density of several per square degree per unit redshift.

Figure 17 shows that the τCDM model is less able to accommodate the existence of these $z > 1$ clusters. The central temperatures correspond to surface densities of 1 cluster 1000 deg^{-2} per unit redshift, a factor 100 times more dilute than the ΛCDM values. Given that only 40 such clusters would be expected on the whole sky between redshifts 1 and 2, it would be remarkable that two would already be identified by these observations.

At the most dilute sky surface density plotted in these figures, each filled circle represents the hottest or most massive cluster within its 0.1 wide redshift bin. Even at this highest rank, the variance in the discrete sample SSDC values remains remarkably small. An exception is the unusual ΛCDM cluster at $z = 1.04$. This monster lies nearly a factor of 2 above the Jenkins model expectations, and its deviation is extreme compared to that displayed by values at the same source density and other redshifts. We note that its expected temperature of 21 keV exceeds that of the hottest known cluster 1E 0657$-$56 at $z = 0.296$, with $kT = 17.4 \pm 2.5$ keV (Tucker et al. 1998), shown as the asterisk in Figures 16 and 17.

As the hottest known cluster, it is natural to expect 1E 0657$-$56 to lie at the extreme end of the surface density distribution in the redshift range 0.2–0.3. That is indeed the outcome of comparing its location to ΛCDM expectations in Figure 16. For the case of τCDM, its existence is more troublesome, but given the combination of T calibration uncertainty and scatter demonstrated by the first-ranked values of the discrete sample, this system is consistent at the $\sim 2\,\sigma$ level with the τCDM expectations. A similar statement of significance can be made for the comparably hot and more distant cluster RX J1347$-$1145, with $kT = 14.48^{+1.76}_{-1.46}$ keV (Ettori, Allen, & Fabian 2001) at $z = 0.451$. This analysis does not support the interpretation of Ettori et al. (2001) that the existence of RX J1347$-$1145 alone can be used to place an upper limit on the matter density parameter $\Omega_m < 0.5$.

To summarize, interpretation of distant cluster counts is complicated by uncertainty in σ_8, variation of which can lead to large factor changes in yield, as well as uncertainty due to possible evolution in β and other aspects of astrophysical evolution. If a constant β assumption is valid for ΛCDM, then $\sim$8 keV clusters at $z = 1.2$–1.3 should be as numerous on the sky as those lying at $z = 0.1$–0.2.

6. SUMMARY OF ΛCDM EXPECTATIONS

Given the increasing likelihood that the ΛCDM model is an accurate representation of our universe (Pryke et al. 2002; Netterfield et al. 2002), we provide here a brief summary and discussion of the characteristics of its cluster population:

Coma mass systems.—The population of clusters with M_{200} in excess of $10^{15}\,h^{-1}\,M_\odot$ is potentially numerous, but not overwhelmingly so. With $\sigma_8 = 0.9$, 400 Comas are expected on the whole sky (Fig. 8), but that number ranges between 40 and 2000 as σ_8 is varied within its 90% confidence limits. The median redshift of this sample is expected to be $z_{\rm med} = 0.48$, nearly independent of σ_8. Detection of Coma equivalents at $z > 1$ in excess of 0.003 deg^{-2} ($\sim$120 across the sky) would rule out ΛCDM at 95% confidence. A complete sample of these objects could be obtained with an all-sky X-ray imaging survey only moderately more sensitive than the *ROSAT* All-Sky Survey (Böhringer et al. 2001). Such a survey would be unique in being the first to be *absolutely complete*, meaning complete in identifying *all* members of a class of astrophysical objects within the finite volume of our past light cone.

Hot X-ray clusters.—A characteristic feature of the ΛCDM model is that the hottest clusters populate the sky at nearly fixed surface density over a broad redshift interval (Fig. 16). This implies a testable prediction of a nearly flat redshift distribution, within $z \simeq 0.2$–1, for a temperature-limited sample identified in a fixed angular survey area. Within the 10,000 deg^2 SDSS area, one 8 keV cluster is expected to lie at $z \geq 2$.

Clusters at $z \sim 3$.—Looking to higher redshifts, clusters with $M_{200} > 10^{14}\,h^{-1}\,M_\odot$ and rest-frame $kT > 4$ keV (apparent $kT \gtrsim 1$ keV) should exist at the level of 1 cluster 100 deg^{-2} per unit redshift under the default σ_8 and β normalizations (Fig. 16). On the order of 100 such clusters are to be expected within the SDSS survey area in the redshift interval 2.5–3.5. Roughly 10 clusters will have rest-frame $kT > 5$ keV and $z > 3$. The vicinity of bright quasars may be a natu-

ral place to search for these systems. Verification of a hot ICM at these redshifts would benefit from the large collecting area of the planned Constellation-X Observatory.

Clusters at $z \lesssim 0.5$.—The SDSS and 2dF optical survey will provide large numbers of clusters selected in redshift space and extending to redshifts $z \sim 0.5$. Although these samples offer an opportunity to place more sensitive constraints on σ_8, a number of systematic effects, such as biases in the selection process and the mapping between properties measured in redshift space (optical richness or velocity dispersion) and underlying cluster mass M, must first be carefully calibrated. Such systematic effects can be profitably studied by combining semianalytic models of galaxy formation with N-body models of dark matter halo evolution (see, e.g., Springel et al. 2001). An X-ray imaging survey to bolometric flux 10^{-14} ergs^{-1} cm^{-2}, capable of identifying all clusters with $M_{200} > 10^{14}\ h^{-1}\ M_\odot$ within $z = 0.4$ (assuming a nonevolving L_X-T relation) would provide the ability to separate truly deep potential wells from redshift space superpositions of smaller systems (Frenk et al. 1990).

ICM temperature evolution.—In predicting that the redshift distribution of hot clusters at fixed sky surface density is flat over observationally accessible redshifts, we have implicitly assumed that the X-ray temperature and mass follow the virial relation $T \propto [H(z)M_{200}]^{2/3}$. It is important to pursue high-resolution imaging and spectroscopy of known high-redshift clusters with *Chandra* and *XMM* in order to test whether more complex heating and cooling processes may be occurring, particularly at high redshift. Such processes would affect attempts to determine the geometry of the universe through the X-ray size-temperature relation (Mohr & Evrard 1997; Mohr et al. 2000).

Precise parameter estimation.—The accuracy of constraints on σ_8 from the cluster temperature function is fundamentally limited by the error in normalization of the mass-temperature relation of hot clusters (eq. [13]); 1% errors on σ_8 will require knowing the absolute mass scale of clusters to better than 3%. This challenging prospect is currently beyond the capabilities of direct computational modeling and traditional observational approaches, such as mass estimates based on hydrostatic equilibrium. Weak gravitational lensing, especially in the form of "field" lensing (see Mellier & van Waerbeke 2002 for a review), appears the most promising approach; for example, Hoekstra et al. (2002) find $\sigma_8 = 0.81^{+0.14}_{-0.19}$ at 95% confidence from analysis of relatively bright (limiting magnitude $R_C = 24$) galaxies in Canada-France-Hawaii Telescope and Cerro Tololo Inter-American Obervatory fields covering 24 deg^2. Imposing such constraints as priors will focus future studies on breaking existing degeneracies between dark matter/dark energy densities and astrophysical evolution.

7. CONCLUSIONS

We present analysis of a pair of gigaparticle simulations designed to explore the emergence of the galaxy cluster population in large cosmic volumes of flat world models dominated by matter energy density (τCDM) and a cosmological constant (ΛCDM). Besides shear scale, these Hubble volume simulations are unique in their production of sky survey catalogs that map structure of the dominant dark matter component over large solid angles and to depths $z \simeq 1.5$ and beyond. Application of an SO cluster-finding algorithm to the sky survey and fixed epoch simulation output results in discrete samples of millions of clusters above the mass scale of galaxy groups ($5 \times 10^{13}\ h^{-1}\ M_\odot$). These samples form the basis of a number of studies; we focus here on precise calibration of the mass function and on systematic uncertainties in cosmological parameter determinations caused by imprecise determination of the absolute mass scale of clusters. A summary of our principal findings is as follows:

1. We calibrate the SO(200) mass function to the Jenkins form with resulting statistical precision of better than 3% in number for masses between $10^{13.5}$ and $10^{15.3}\ h^{-1}\ M_\odot$. A preliminary estimate of the overall theoretical uncertainty in this calibration is approximately 20%.

2. We fit the local temperature function under the assumption that the disordered kinetic energy in dark matter predicts the ICM thermal temperature, leading to specific energy ratios $\beta_\Lambda = (0.92 \pm 0.06)(\sigma_8/0.9)^{5/3}$ and $\beta_\tau = (1.10 \pm 0.06)(\sigma_8/0.6)^{5/3}$. For the ΛCDM model, $\sigma_8 = 1.04$ is required to match the value $\beta_{\rm sim} = 1.17$ preferred by gasdynamic simulations of ICM evolution.

3. Based on the Jenkins form for the mass function, we derive transformations of the discrete cluster sample that mimic variation in σ_8. Using these transformations, we show that the redshift distribution of mass-limited samples is a more powerful cosmological diagnostic than cluster counts; the median redshift of clusters more massive than $10^{14}\ h^{-1}\ M_\odot$ in a single 10 deg^2 field of a ΛCDM cosmology can rule out τCDM at a minimum of 95% confidence.

4. The ΛCDM model, under conservative assumptions for intracluster gas evolution, is consistent with high-redshift cluster samples observed in the X-ray–selected EMSS and RDCS.

5. The statistics of sky surface density characteristic (SSDC) mass and temperature are introduced to more naturally account for observational and theoretical uncertainties in measured physical scales. The ΛCDM model predicts flat redshift behavior in the SSDC temperature; a randomly chosen 8 keV cluster on the sky is nearly equally likely to lie at any redshift in the interval 0.2–1.2.

6. With $\sigma_8 = 0.9$, the ΛCDM model predicts roughly 400 Coma mass ($10^{15}\ h^{-1}\ M_\odot$) clusters across the sky at all redshifts, with the most distant lying just beyond $z = 1$. Pushing σ_8 to its 95% confidence upper limit, the ΛCDM model could accommodate up to 120 Coma equivalents on the sky at $z > 1$.

Larger and deeper cluster samples with accurate determinations of temperature or mass will lead to improved constraints on cosmological and astrophysical parameters. The developing 2dF survey and SDSS will provide large numbers of clusters with galaxy velocity dispersion $\sigma_{\rm gal}$ serving as a temperature measure and optical richness $N_{\rm gal}$ serving as a surrogate for mass. Gravitational lensing mass estimates will also be possible for co-added ensembles of clusters (Sheldon et al. 2001). Extracting cosmological information from these data will require likelihoods such as $p(\sigma_v|\sigma_{\rm gal})$ or $p(M|N_{\rm gal})$. The challenge to the theoretical community will be to model these likelihoods at a level of precision warranted by the large data sets. Almost certainly, the theoretical uncertainty associated with this aspect of the modeling will dominate statistical errors since samples of many thousands, perhaps tens of thousands, of groups and clusters will be available in the complete 2dF survey and

SDSS. By imposing external constraints on selected parameters and requiring model consistency across independent observables (e.g., submillimeter, optical, and X-ray), constraints on cosmological and astrophysical parameters can be derived from a number of alternate paths.

Valuable complementary information is available at X-ray wavelengths. An X-ray imaging survey reaching to limiting flux $\sim 3 \times 10^{-14}$ ergs s^{-1} cm^{-2} in the 0.5–6 keV band would be capable of detecting a cluster with 6 keV rest-frame temperature to $z = 1$ in either of the cosmologies studied here, assuming a nonevolving L_X-T relation. The redshift distribution of such a sample would be a powerful cosmological diagnostic, as long as astrophysical evolution of the ICM could be sufficiently well constrained. A program of deep pointed observations with *Chandra* and *XMM* (to constrain the astrophysical evolution) coupled with a deep X-ray imaging survey covering a significant portion of the SDSS area (to identify a large cluster population in redshift space) would be a powerful combination. SZ surveys over large solid angle with bolometer arrays could play a similar role to an X-ray imaging mission, and interferometric arrays will probe to smaller masses and higher redshifts than can be achieved by any current search techniques. Ultimately, the combination of *all* these approaches, along with deep, optical imaging and spectroscopy, will allow determinations of cosmological parameters to be made not only more precise, by shear statistical weight, but also be made more accurate by improving our understanding of the astrophysical processes that govern the evolution of the visible components of clusters.

This work was funded by the PPARC in the UK, the Max-Planck Society in Germany, NSERC in Canada, NASA and NSF in the US, and NATO in all the countries involved. Some of this work was carried out as part of the EU Network for Galaxy Formation and Evolution. C. S. F. acknowledges a Leverhulme Research Fellowship. We thank the staff of the Rechenzentrum Garching for outstanding computational support. A. E. E. acknowledges support from NSF AST 98-03199 and NASA NAG 5-7108, clarifying conversations with A. Blanchard and J. Bartlett, and the benefits of the Scientific Visitor Program at Carnegie Observatories in Pasadena.

APPENDIX A

CLUSTER-FINDING DETAILS AND COMPLETENESS CHECKS

The cluster-finding algorithm that produced the catalogs in this paper begins by generating a density estimate for each particle using the distance to its eighth nearest neighbor (Casertano & Hut 1985), equivalent to Lagrangian filtering on a mass scale $2 \times 10^{13}\, h^{-1}\, M_\odot$. Sorting density values in decreasing order provides a list of potential sites for cluster centers. The list is pruned by eliminating particles whose densities lie below the threshold $\Delta\rho_c(z)$. Beginning with the first member of the sorted list, a sphere of radius r_Δ enclosing mass M_Δ is defined about that particle so that the enclosed density $\rho \equiv 3M_\Delta/4\pi r_\Delta^3 = \Delta\rho_c(z)$. Particles lying within this sphere are recorded as members of this group and are removed from the list of potential cluster centers. The process is repeated sequentially, centering on the next available particle in the list ordered by decreasing density, until the list is exhausted. Particles may belong to more than one group, but the center of a given group never lies within the spherical boundary of another group.

In analyzing SO(180) and mean SO(324) populations of the τCDM and ΛCDM models, respectively, J01 noted a problem of incompleteness in the SO cluster-finding algorithm at particle counts $\lesssim 100$. Resolution tests in J01 indicated that space densities of groups comprised of 20 particles could be underestimated by $\sim 30\%$. We employ here an independent SO algorithm with improved completeness properties at small numbers of particles. Figure 18 compares the SO(180) and mean SO(324) abundance functions (for τCDM and ΛCDM, respectively) at $z = 0$ based on the new algorithm to the fits published in Appendix B of J01.

In the figure, the thick solid lines show J01 functional fits while the thin solid and dotted lines show discrete mass functions derived with the algorithm employed here. The dot-dashed line is the discrete τCDM mass function derived by J01 using the previous SO algorithm. The top panel shows the percent deviation between the discrete sample measurements and the fit expectations.

For the τCDM case, both the old and new algorithms compare well against each other and against the fit above $\sim 10^{15}\, h^{-1}\, M_\odot$. At lower masses, the J01 algorithm displays an increasing underestimate in number density with respect to the fit, approaching a 30% underestimate at the mass limit $5 \times 10^{13}\, h^{-1}\, M_\odot$ used in this work. The new SO algorithm (*dotted line*) displays a similar qualitative trend, but the underestimate is reduced to $\lesssim 10\%$ in amplitude. A similar trend is seen for the new algorithm in the ΛCDM case, in which the number density lies $\sim 12\%$ lower than the J01 fit expectations. This analysis indicates that the amplitude A derived from fitting the space density to the Jenkins form, to equation (10), may be biased low by $\sim 10\%$ at masses below $\sim 10^{15}\, h^{-1}\, M_\odot$.

A further check of resolution effects is made by directly comparing the HV mass function to one derived from smaller volumes with improved mass resolution. We do this for SO(200) clusters in the ΛCDM model at $z = 0$, using data from the 256^3 particle simulation of a $239.5\, h^{-1}$ Mpc region from Jenkins et al. (1998). The new SO(200) algorithm is used to identify clusters in the same manner as done in the HV simulation. The cosmological parameters for the models are the same, except for a slight difference in the power spectrum used to generate the initial conditions, whereas the particle mass in the 256^3 particle simulation is a factor of 32 times smaller than that used in the HV computations.

Figure 19 shows the cumulative number of clusters found in the 256^3 particle simulation (*dotted line*) along with the number expected based on the $z = 0$ HV population (*solid line*). Vertical bars on the HV results show the range in number derived from dividing the HV volume into 1728 independent cubes of side $250\, h^{-1}$ Mpc and rescaling the counts in each cube to a $(239.5\, h^{-1}$ Mpc$)^3$ volume. The inset shows the correlation between counts above 5×10^{13} and $3 \times 10^{14}\, h^{-1}\, M_\odot$ within the subvolumes.

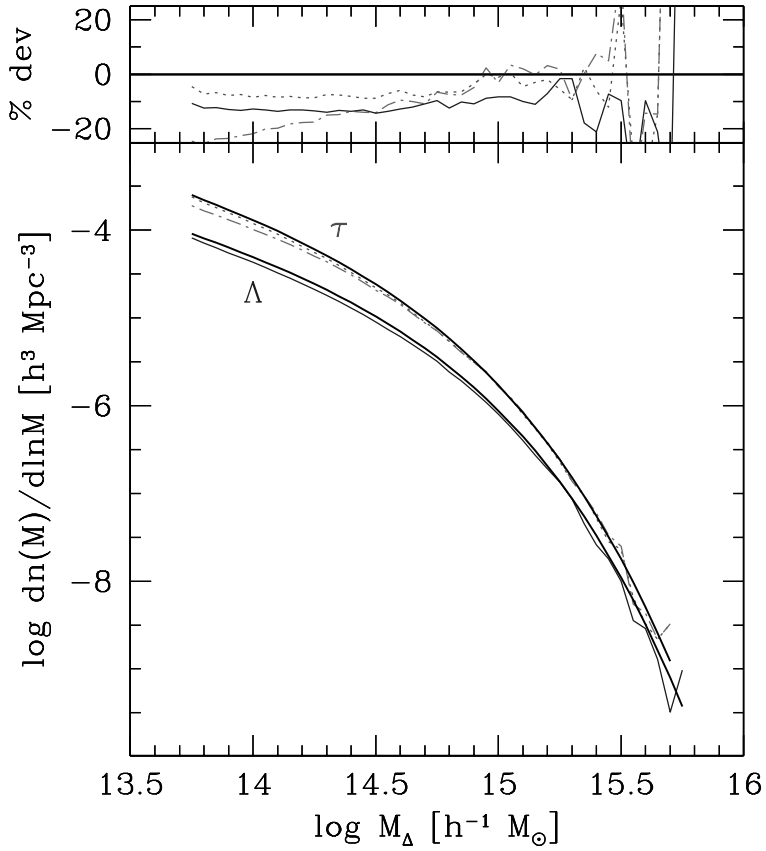

FIG. 18.—Differential SO mass functions at $z = 0$ compared to the fits published in J01. In the lower panel, thick lines are the J01 expectations (from their Appendix B) for τCDM at $\Delta = 180$ (*upper curve*) and ΛCDM at mean $\Delta = 324$ (critical $\Delta = 97.2$, *lower curve*). The ΛCDM simulation data are shown by the slightly jagged solid curve. Two simulation results are shown for τCDM—the dot-dashed line reflects the SO algorithm used by J01, and the dotted line shows results of the algorithm used in this work. The upper panel displays the percent deviation in number density between the HV simulation data and the J01 model fits. [*See the electronic edition of the Journal for a color version of this figure.*]

The small-volume simulation result is inconsistent with the HV distribution; the count distribution shows agreement at the 98% level at $3 \times 10^{14}\ h^{-1}\ M_{\odot}$, but the 5×10^{13} count is $\sim$0.5% higher than the maximum of the HV distribution and $\sim$20% above the mean.

These findings, along with the slight discrepancy in predicted versus measured counts in the τCDM octant surveys (Fig. 7) lead to a conservative estimate of the systematic theoretical uncertainty in the number density of clusters above $10^{14}\ h^{-1}\ M_{\odot}$ to be 20%. Future studies, in particular those that cross-calibrate results for a particular cosmology modeled by different simulation teams, are needed to better assess the overall accuracy of this model of the mass function.

APPENDIX B

MASS SCALE RENORMALIZATION

The mass scale of clusters at fixed space density is uncertain, both theoretically and empirically, for reasons discussed in § 1. The lack of a uniquely defined scale motivates a model that would transform the JMF fit parameters derived in § 3.3 to values appropriate for a redefined mass scale. As an example, we develop here a model to estimate the SO mass function fit parameters for threshold values $\Delta \neq 200$. The method is similar to that used in § 5.2 to effectively vary σ_8 within the discrete cluster samples.

We have chosen a convention in which a spherical density threshold $\Delta = 200$ defines cluster masses M. A choice $\Delta \neq 200$ would lead to a new mass M' for each cluster related to the original by some factor

$$M' = Me^{\mu} . \tag{B1}$$

The space density of a set of *disjoint* clusters is fixed, implying

$$n(M')d\ln M' = n(M)d\ln M . \tag{B2}$$

This condition, with equation (B1), when used with the space density, equation (10), leads to a relation between JMF

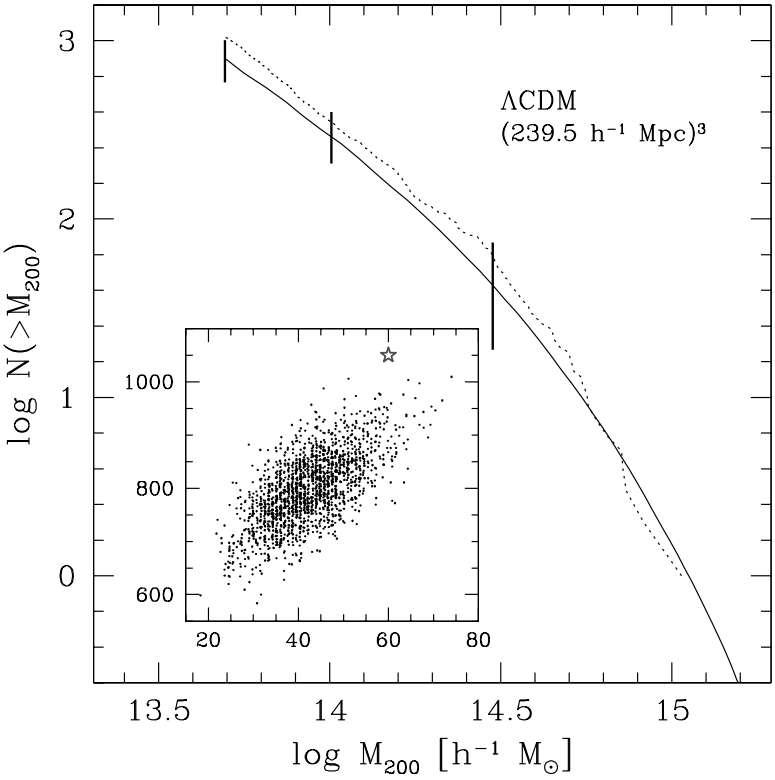

FIG. 19.—Cumulative number of clusters within the volume indicated, scaled from the full $z = 0$ HV simulation (*solid line*) and from a single realization of a $(239.5\ h^{-1}\ \mathrm{Mpc})^3$ volume (Jenkins et al. 1998; *dotted line*) for the ΛCDM cosmology. The vertical lines show the entire range of counts above masses 5×10^{13}, 10^{14}, and $3 \times 10^{14}\ h^{-1}\ M_\odot$ derived from subsampling 1728 cubic subvolumes of side $250\ h^{-1}$ Mpc within the HV realization and scaling to $239.5\ h^{-1}$ Mpc. The inset plots the correlation of counts above 3×10^{14} (*x*-axis) and 5×10^{13} (*y*-axis) derived from the subvolumes. The star indicates the Jenkins et al. (1998) values. [*See the electronic edition of the Journal for a color version of this figure*.]

parameters

$$A' = Ae^{\mu}, \qquad B' = B - \alpha_{\mathrm{eff}}(M)\mu \tag{B3}$$

to first order in μ.

The factor μ can be calculated from an assumed mass profile. We use the form introduced by Navarro et al. (1996),

$$M(x) = \frac{800\pi}{3}\rho_c r_{200}^3 \left[\frac{\ln(1+cx) - cx/(1+cx)}{\ln(1+c) - c/(1+c)}\right], \tag{B4}$$

where $x = r/r_{200}$ is a scaled radius and c is a concentration parameter. *N*-body simulations suggest $c \simeq 5$ at masses near 10^{15} h^{-1} Mpc for the cosmologies studied here (Navarro et al. 1996; Frenk et al. 1999; Jing 2000; Bullock et al. 2001).

Figure 20 shows the results of applying equation (B3) to critical contrasts $\Delta = 97.2$ and 500 for the ΛCDM model, assuming $c = 5$. The logarithmic shifts in mass scale are $\mu = 0.093$ and -0.141, respectively. The agreement between the predicted and measured values is quite good. At $\Delta = 97.2$ (equivalent to the mean contrast of 324 used by J01), the bin-averaged mean fractional error and dispersion (for bins with 10% or less Poisson uncertainty) are only 4.1% and 3.8%. At $\Delta = 500$, the mean is -14.5% and dispersion 4.9%.

APPENDIX C

CLUSTER CATALOGS

The SO(200) cluster catalogs derived from the sky survey and $z = 0$ snapshot outputs of the simulations are included here as electronic tables. In the print edition, Tables 6-17 provide a truncated listing of the 10 most massive clusters for each survey. Electronic versions list all clusters resolved above a mass limit of 22 particles ($5 \times 10^{13}\ h^{-1}\ M_\odot$), the numbers of which are listed in Table 5. Tables 6–11 are ΛCDM simulation catalogs from the $z = 0$ snapshot, the combined PO and XW sky surveys, and the NO, VS, MS, and DW sky surveys, respectively. Tables 12–17 provide the same for τCDM, with the exception that there is no extended wedge associated with the PO survey of this model (see Table 2).

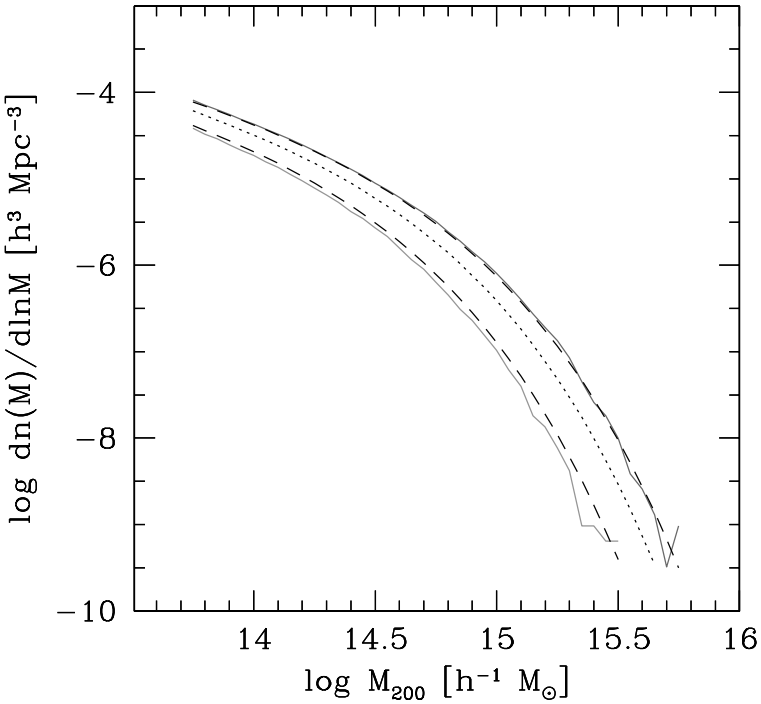

FIG. 20.—Critical SO(500) and SO(97.2) mass functions (*top and bottom*, respectively) at $z = 0$ for ΛCDM. The solid lines are measured from the HV simulation, while the dashed lines are predictions based on rescaling the SO(200) JMF fit (*dotted line*), assuming a Navarro et al. 1996 profile with concentration parameter $c = 5$. [*See the electronic edition of the Journal for a color version of this figure*.]

Column entries give the mass M_{200} (in units of $10^{15}\,h^{-1}\,M_{\odot}$), redshift (for sky survey data) derived from Hubble flow and the radial peculiar velocity, one-dimensional velocity dispersion σ_v determined from a three-dimensional average (in units of km s^{-1}), position in comoving coordinates (in units of h^{-1} Gpc), and peculiar velocity (in units of km s^{-1}). The position is defined as the location of the particle having the smallest distance to its eighth neighboring particle (see Appendix A), and the peculiar velocity is defined by the mass-weighted mean within r_{200}.

TABLE 6
CLUSTERS IN THE ΛCDM $z = 0$ SNAPSHOT SURVEY

M_{200} ($\times 10^{15}\,h^{-1}\,M_{\odot}$)	σ (km s^{-1})	x (h^{-1} Gpc)	y (h^{-1} Gpc)	z (h^{-1} Gpc)	v_x (km s^{-1})	v_y (km s^{-1})	v_z (km^{-1})
4.7745	1795	2.27792	0.44894	0.54195	−90	153	−6
4.7475	1866	2.03410	0.91683	0.44397	269	46	727
4.2840	1781	1.74103	2.84553	1.40265	87	−52	−154
3.9645	1632	0.96734	0.65102	2.32061	63	312	−282
3.8227	1891	1.75213	0.72151	1.80426	380	−90	−279
3.4920	1665	1.50312	1.77336	2.19206	−26	1	−17
3.3772	1531	1.21292	2.12486	0.27272	−434	−228	−821
3.3592	1583	2.50579	2.18682	0.31021	−183	588	174
3.3187	1519	2.07928	2.97238	1.91753	−532	−531	−156
3.2602	1566	0.38232	1.70524	0.62298	−228	257	98

NOTE.—Table 6 is published in its entirety in the electronic edition of the *Astrophysical Journal*. A portion is shown here for guidance regarding its form and content.

TABLE 7

CLUSTERS IN THE ΛCDM PO+XW SKY SURVEY

M_{200} ($\times 10^{15}\,h^{-1}\,M_\odot$)	Redshift	σ (km s^{-1})	x (h^{-1} Gpc)	y (h^{-1} Gpc)	z (h^{-1} Gpc)	v_x (km s^{-1})	v_y (km s^{-1})	v_z (km s^{-1})
2.1465	1.04210	1740	2.27834	0.44795	0.54248	229	319	−99
1.9035	0.49167	1490	0.48208	1.20790	0.20341	287	−806	−725
1.8337	0.48731	1473	1.25433	0.30248	0.12419	300	−692	13
1.6245	0.48492	1440	1.25607	0.30110	0.12310	−520	45	327
1.6132	0.74772	1389	0.38256	1.70412	0.62232	171	−58	192
1.5052	0.48217	1339	1.00142	0.47311	0.64768	−177	670	268
1.4850	0.63925	1309	1.21259	0.74437	0.79747	−4	−6	406
1.4265	0.33432	1338	0.15125	0.88516	0.24984	−533	−287	−210
1.3927	0.26386	1273	0.62241	0.37143	0.16475	283	50	−310
1.3860	0.95680	1403	1.28228	0.28511	1.81830	−107	−259	41

NOTE.—Table 7 is published in its entirety in the electronic edition of the *Astrophysical Journal*. A portion is shown here for guidance regarding its form and content.

TABLE 8

CLUSTERS IN THE ΛCDM NO SKY SURVEY

M_{200} ($\times 10^{15}\,h^{-1}\,M_\odot$)	Redshift	σ (km s^{-1})	x (h^{-1} Gpc)	y (h^{-1} Gpc)	z (h^{-1} Gpc)	v_x (km s^{-1})	v_y (km s^{-1})	v_z (km s^{-1})
1.8720	0.47097	1357	0.78598	0.89484	0.40376	−13	365	−193
1.6762	0.45872	1332	0.25973	1.14905	0.34105	−128	508	−150
1.5750	0.39013	1393	0.50888	0.89409	0.29059	−106	−92	−379
1.4985	0.36176	1308	0.54647	0.73774	0.40355	−467	−203	−432
1.4625	0.09295	1230	0.11250	0.20762	0.13595	114	63	68
1.4602	0.21513	1254	0.13535	0.45678	0.38800	−624	336	−46
1.4422	0.23629	1209	0.21785	0.32614	0.54597	41	299	−195
1.4310	0.84337	1304	1.25924	0.15777	1.59600	−158	−124	27
1.3612	0.25340	1225	0.35217	0.57399	0.23736	−38	458	−21
1.3567	0.24869	1277	0.68191	0.11578	0.14755	46	−19	−1027

NOTE.—Table 8 is published in its entirety in the electronic edition of the *Astrophysical Journal*. A portion is shown here for guidance regarding its form and content.

TABLE 9

CLUSTERS IN THE ΛCDM VS SKY SURVEY

M_{200} ($\times 10^{15}\,h^{-1}\,M_\odot$)	Redshift	σ (km s^{-1})	x (h^{-1} Gpc)	y (h^{-1} Gpc)	z (h^{-1} Gpc)	v_x (km s^{-1})	v_y (km s^{-1})	v_z (km s^{-1})
3.7710	0.36705	1849	0.77855	1.94855	2.04204	−179	109	−38
2.3985	0.12317	1427	1.66806	1.18289	1.50177	−100	−204	−269
2.1847	0.31494	1513	1.16682	1.78942	0.74591	−276	55	−309
2.1352	0.22786	1510	1.83355	0.95563	1.60533	228	−71	352
2.0407	0.25998	1427	1.69566	2.12671	1.17188	−529	84	−410
2.0385	0.27780	1536	1.14664	2.02703	1.04228	−73	94	220
1.9957	0.21552	1393	1.20062	1.88904	1.87100	60	546	−365
1.9282	0.17104	1473	1.83406	1.48791	1.14040	367	−434	−99
1.9260	0.38687	1515	1.99907	1.19847	2.37855	294	−141	207
1.9237	0.21232	1425	1.62686	0.92821	1.34563	203	−10	−516

NOTE.—Table 9 is published in its entirety in the electronic edition of the *Astrophysical Journal*. A portion is shown here for guidance regarding its form and content.

TABLE 10

CLUSTERS IN THE ΛCDM MS SKY SURVEY

M_{200} ($\times 10^{15}\,h^{-1}\,M_\odot$)	Redshift	σ (km s^{-1})	x (h^{-1} Gpc)	y (h^{-1} Gpc)	z (h^{-1} Gpc)	v_x (km s^{-1})	v_y (km s^{-1})	v_z (km s^{-1})
3.0622	0.12208	1765	1.61387	1.63047	1.81743	−135	−43	−404
2.9452	0.20045	1583	1.13968	1.94410	1.59070	37	−315	−414
2.7225	0.21132	1724	1.77946	1.14258	1.88827	41	−144	941
2.6640	0.26329	1622	1.50191	1.77218	2.19369	434	317	−245
2.3692	0.39004	1536	1.21250	0.74412	0.79839	−210	0	684
2.2320	0.53759	1482	1.20256	2.12932	0.26569	636	−375	138
2.1690	0.48039	1534	1.28226	0.28481	1.81857	55	−597	114
2.0925	0.54800	1465	0.38300	1.70434	0.62229	−215	29	239
2.0272	0.47799	1414	1.16678	1.69964	0.28919	308	159	−474
1.9147	0.41372	1393	0.49259	1.31877	1.03747	86	548	−522

NOTE.—Table 10 is published in its entirety in the electronic edition of the *Astrophysical Journal*. A portion is shown here for guidance regarding its form and content.

TABLE 11

CLUSTERS IN THE ΛCDM DW SKY SURVEY

M_{200} ($\times 10^{15}\,h^{-1}\,M_\odot$)	Redshift	σ (km s^{-1})	x (h^{-1} Gpc)	y (h^{-1} Gpc)	z (h^{-1} Gpc)	v_x (km s^{-1})	v_y (km s^{-1})	v_z (km s^{-1})
1.2667	0.35165	1194	0.52955	0.51554	0.62439	236	159	160
0.7425	0.63063	1020	0.89636	1.04111	0.84907	58	−57	21
0.7335	0.54100	1078	0.83017	0.88976	0.74354	−346	−269	−328
0.6952	0.86474	1077	1.26522	1.12729	1.20595	−417	−122	217
0.6795	0.23262	883	0.42833	0.36816	0.34631	184	−40	−201
0.6277	0.49817	968	0.79520	0.73876	0.75309	24	340	−103
0.6210	0.61920	1075	0.87578	0.91529	0.96280	−130	−498	540
0.5872	0.16708	833	0.29741	0.28511	0.25289	406	−169	−255
0.5557	0.24148	766	0.37255	0.44021	0.38042	331	−714	−279
0.5512	0.52327	998	0.76163	0.87778	0.75294	−389	−179	−160

NOTE.—Table 11 is published in its entirety in the electronic edition of the *Astrophysical Journal*. A portion is shown here for guidance regarding its form and content.

TABLE 12

CLUSTERS IN THE τCDM $z = 0$ SNAPSHOT SURVEY

M_{200} ($\times 10^{15}\,h^{-1}\,M_\odot$)	σ (km s^{-1})	x (h^{-1} Gpc)	y (h^{-1} Gpc)	z (h^{-1} Gpc)	v_x (km s^{-1})	v_y (km s^{-1})	v_z (km s^{-1})
4.8840	1912	1.60532	0.11171	1.05673	−273	241	−141
4.8707	1946	1.76731	0.09581	0.98359	206	229	−728
4.7597	1907	0.46288	1.83931	0.73075	402	598	−359
4.3290	1787	1.06007	1.25750	0.15836	195	−102	160
4.3246	1816	0.62941	0.32143	0.59557	−120	462	−43
4.1270	1655	0.18549	1.04133	1.38113	125	−584	−549
4.0448	1820	1.40794	0.55788	0.85002	−596	282	−236
3.8473	1734	0.24495	0.63610	0.51995	169	473	235
3.5209	1688	1.59185	0.02998	1.51849	−21	−1044	−78
3.5187	1569	0.54769	0.03614	1.24131	−125	524	−62

NOTE.—Table 12 is published in its entirety in the electronic edition of the *Astrophysical Journal*. A portion is shown here for guidance regarding its form and content.

TABLE 13

CLUSTERS IN THE τCDM PO SKY SURVEY

M_{200} ($\times 10^{15}\,h^{-1}\,M_\odot$)	Redshift	σ (km s^{-1})	x (h^{-1} Gpc)	y (h^{-1} Gpc)	z (h^{-1} Gpc)	v_x (km s^{-1})	v_y (km s^{-1})	v_z (km s^{-1})
2.2333	0.15351	1635	0.02751	0.34796	0.21763	−155	234	84
1.9869	0.20570	1568	0.10704	0.52032	0.07637	−219	−55	−49
1.7671	0.39740	1512	0.62955	0.31885	0.59612	−123	640	−105
1.4208	0.26994	1345	0.18684	0.32731	0.55685	934	−132	219
1.3942	0.01660	1259	0.02224	0.05106	0.01156	−742	−559	77
1.2920	0.29180	1311	0.09007	0.52090	0.49083	−153	−70	39
1.2898	0.08068	1246	0.21347	0.08099	0.01491	122	−443	−133
1.2521	0.27828	1341	0.58237	0.37616	0.02971	−206	150	35
1.1500	0.25740	1307	0.43210	0.35366	0.33809	−507	−135	33
1.0811	0.19157	1201	0.42661	0.26000	0.09128	−478	−105	−160

NOTE.—Table 13 is published in its entirety in the electronic edition of the *Astrophysical Journal*. A portion is shown here for guidance regarding its form and content.

TABLE 14

CLUSTERS IN THE τCDM NO SKY SURVEY

M_{200} ($\times 10^{15}\,h^{-1}\,M_\odot$)	Redshift	σ (km s^{-1})	x (h^{-1} Gpc)	y (h^{-1} Gpc)	z (h^{-1} Gpc)	v_x (km s^{-1})	v_y (km s^{-1})	v_z (km s^{-1})
1.8781	0.16574	1489	0.08750	0.34930	0.25921	532	−14	−310
1.6650	0.23534	1613	0.17937	0.04762	0.57891	−102	−429	−661
1.6228	0.40003	1540	0.64304	0.36559	0.55891	−6	475	93
1.5873	0.23482	1433	0.19753	0.03359	0.57222	−426	−150	−519
1.4119	0.13676	1456	0.15879	0.33140	0.02784	70	401	403
1.2388	0.08092	1148	0.13108	0.17990	0.05517	−93	166	−475
1.1566	0.14827	1301	0.23406	0.24841	0.20322	599	505	−569
1.1433	0.14885	1309	0.15585	0.14787	0.33972	36	−297	142
1.1255	0.13588	1194	0.25388	0.00900	0.26156	275	118	572
1.0922	0.05791	1091	0.03287	0.13919	0.07741	23	353	197

NOTE.—Table 14 is published in its entirety in the electronic edition of the *Astrophysical Journal*. A portion is shown here for guidance regarding its form and content.

TABLE 15

CLUSTERS IN THE τCDM VS SKY SURVEY

M_{200} ($\times 10^{15}\,h^{-1}\,M_\odot$)	Redshift	σ (km s^{-1})	x (h^{-1} Gpc)	y (h^{-1} Gpc)	z (h^{-1} Gpc)	v_x (km s^{-1})	v_y (km s^{-1})	v_z (km s^{-1})
2.5530	0.08805	1595	1.23821	1.06196	0.96259	−18	−331	78
2.5108	0.15568	1622	1.41088	0.90971	0.98357	−261	−24	−177
2.2333	0.15351	1635	1.02751	1.34795	1.21762	−155	234	84
1.9869	0.20570	1568	1.10704	1.52032	1.07637	−218	−55	−49
1.9358	0.17072	1389	0.96303	1.00973	0.54585	−48	394	126
1.8937	0.16180	1570	0.57437	0.89833	1.00483	410	211	−184
1.8781	0.16574	1489	0.91249	0.65070	0.74078	−532	14	311
1.7671	0.39740	1513	1.62955	1.31885	1.59612	−120	638	−106
1.7560	0.37118	1547	1.46201	0.83718	1.73270	127	852	−638
1.7405	0.24550	1491	0.92007	1.16642	1.59436	−310	137	81

NOTE.—Table 15 is published in its entirety in the electronic edition of the *Astrophysical Journal*. A portion is shown here for guidance regarding its form and content.

TABLE 16

CLUSTERS IN THE τCDM MS SKY SURVEY

M_{200} ($\times 10^{15}\,h^{-1}\,M_\odot$)	Redshift	σ (km s^{-1})	x (h^{-1} Gpc)	y (h^{-1} Gpc)	z (h^{-1} Gpc)	v_x (km s^{-1})	v_y (km s^{-1})	v_z (km s^{-1})
2.8616	0.08778	1619	1.12538	1.09734	0.80682	−359	49	176
2.6662	0.09450	1569	0.83169	1.09487	0.82472	−444	32	−178
2.0446	0.23637	1552	0.69721	1.13044	1.50301	161	−325	514
2.0291	0.23655	1533	1.40187	1.26906	1.36378	−248	−415	427
1.9625	0.36864	1529	0.62959	0.31918	0.59623	−93	539	−159
1.8448	0.37457	1541	1.06066	1.25588	0.15810	20	315	53
1.7960	0.06498	1418	1.04302	1.16623	0.93822	566	268	62
1.7804	0.35602	1629	1.35688	1.63401	1.44111	9	−443	−117
1.7649	0.13530	1456	0.70869	1.17978	0.85280	571	211	141
1.7027	0.13167	1369	0.94757	0.90342	0.65712	205	45	−20

NOTE.—Table 16 is published in its entirety in the electronic edition of the *Astrophysical Journal*. A portion is shown here for guidance regarding its form and content.

TABLE 17

CLUSTERS IN THE τCDM DW SKY SURVEY

M_{200} ($\times 10^{15}\,h^{-1}\,M_\odot$)	Redshift	σ (km s^{-1})	x (h^{-1} Gpc)	y (h^{-1} Gpc)	z (h^{-1} Gpc)	v_x (km s^{-1})	v_y (km s^{-1})	v_z (km s^{-1})
0.5683	0.30774	993	0.41763	0.43087	0.45194	292	69	54
0.5461	0.11396	876	0.19790	0.17877	0.17220	−94	−258	−63
0.4951	0.46020	1001	0.65398	0.57027	0.56948	−842	261	4
0.4484	0.32176	890	0.47050	0.45774	0.42240	210	−75	−31
0.4285	0.28315	837	0.39105	0.38532	0.44474	37	−578	−129
0.4107	0.31961	986	0.47673	0.44308	0.42215	−146	375	11
0.3929	0.18746	818	0.28105	0.30862	0.25462	351	600	−69
0.3441	0.17978	833	0.28576	0.26987	0.26635	−27	34	234
0.3419	0.19586	796	0.29392	0.31370	0.27936	328	150	−391
0.3397	0.51005	894	0.60047	0.61408	0.71184	70	119	190

NOTE.—Table 17 is published in its entirety in the electronic edition of the *Astrophysical Journal*. A portion is shown here for guidance regarding its form and content.

REFERENCES

Annis, J., et al. 2001, BAAS, 198, 26.01
Arnaud, M., & Evrard, A. E. 1999, MNRAS, 305, 631
Bahcall, N. A., & Fan, X. 1998, ApJ, 504, 1
Bahcall, N. A., Fan, X., & Cen, R. 1997, ApJ, 485, L53
Balogh, M. L., Babul, A., & Patton, D. R. 1999, MNRAS, 307, 463
Barbosa, D., Bartlett, J., Blanchard, A., & Oukbir, J. 1996, A&A, 314, 13
Bialek, J., Evrard, A. E., & Mohr, J. J. 2001, ApJ, 555, 597
Birkinshaw, M. 1999, Phys. Rep., 310, 97
Blanchard, A., & Bartlett, J. G. 1998, A&A, 332, L49
Blanchard, A., Sadat, R., Bartlett, J., & Le Dour, M. 2000, A&A, 362, 809
Bode, P., Bahcall, N. A., Ford, E. B., & Ostriker, J. P. 2001, ApJ, 551, 15
Böhringer, H., et al. 2001, A&A, 369, 826
Bond, J. R., Cole, S., Efstathiou, G., & Kaiser, N. 1991, ApJ, 379, 440
Bond, J. R., & Efstathiou, G. 1984, ApJ, 285, L45
Borgani, S., Girardi, M., Carlberg, R. G., Yee, H. K. C., & Ellingson, E. 1999a, ApJ, 527, 561
Borgani, S., Rosati, P., Tozzi, P., & Norman, C. 1999b, ApJ, 517, 40
Bower, R. G. 1997, MNRAS, 288, 355
Bower, R. G., Benson, A. J., Lacey, C. G., Baugh, C. M., Cole, S., & Frenk, C. S. 2001, MNRAS, 325, 497
Bryan, G. L., & Norman, M. L. 1998, ApJ, 495, 80
Bullock, J. S., Kolat, T. S., Sigad, Y., Somerville, R. S., Kravtsov, A. V., Klypin, A. A., Primack, J. R., & Dekel, A. 2001, MNRAS, 321, 559
Burles, S., & Tytler, D. 1998, ApJ, 507, 732
Carlberg, R. G., Yee, H. K. C., & Ellingson, E. 1997, ApJ, 478, 462
Casertano, P., & Hut, P. 1985, ApJ, 298, 80
Cavaliere, A., & Fusco-Femiano, R. 1976, A&A, 49, 137
Cavaliere, A., Menci, N., & Tozzi, P. 1999, MNRAS, 308, 599
Colberg, J., et al. 2000, MNRAS, 319, 209
Colless, M. 2001, MNRAS, 328, 1039
Colombi, S., Szapudi, I., Jenkins, A., & Colberg, J. 2000, MNRAS, 313, 711
Dalton, G. B., Maddox, S. J., Sutherland, W. J., & Efstathiou, G. 1997, MNRAS, 289, 263
David, L. P., Nulsen, P. E. J., McNamara, B. R., Forman, W., Jones, C., Ponman, T., Robertson, B., & Wise, M. 2001, ApJ, 557, 546
Davis, M., Efstathiou, G., Frenk, C. S., & White, S. D. M. 1985, ApJ, 292, 371
de Grandi, S., et al. 1999, ApJ, 514, 148
Donahue, M., Voit, G. M., Gioia, I. M., Luppino, G., Hughes, J. P., & Stocke, J. T. 1998, ApJ, 502, 550
Ebeling, H., Edge, A. C., B öhringer, H., Allen, S. W., Crawford, C. S., Fabian, A. C., Voges, W., & Huchra, J. P. 1998, MNRAS, 301, 881
Ebeling, H., Edge, A. C., & Henry, J. P. 2001, ApJ, 553, 668
Eke, V. R., Cole, S., & Frenk, C. S. 1996, MNRAS, 282, 263
Eke, V. R., Cole, S., Frenk, C. S., & Henry, J. P. 1998, MNRAS, 298, 1145
Ettori, S., Allen, S. W., & Fabian, A. C. 2001, MNRAS, 322, 187
Evrard, A. E. 1990, ApJ, 363, 349
Evrard, A. E., & Henry, J. P. 1991, ApJ, 383, 95
Evrard, A. E., Metzler, C., & Navarro, J. F. 1996, ApJ, 469, 494
Fabian, A. C., Crawford, C. S., Ettori, S., & Sanders, J. S. 2001, MNRAS, 322, L11
Fairley, B. W., Jones, L. R., Scharf, C., Ebeling, H., Perlman, E., Horner, D., Wegner, G., & Malkan, M. 2000, MNRAS, 315, 669
Fan, X., Bahcall, N. A., & Cen, R. 1997, ApJ, 490, L123
Finoguenov, A., Reiprich, T. H., & Böhringer, H. 2001, A&A, 368, 749
Fischer, P., et al. 2000, AJ, 120, 1198
Frenk, C. S., et al. 1999, ApJ, 525, 554
———. 1990, ApJ, 351, 10
Gal, R. R., de Carvalho, R. R., Odewahn, S. C., Djorgovski, S. G., & Magoniner, V. E. 2000, AJ, 119, 12
Gioia, I. M., Henry, J. P., Mullis, C. R., Voges, W., Briel, U. G., Böhringer, H., & Huchra, J. P. 2001, ApJ, 553, L105
Gioia, I. M., & Luppino, G. A. 1994, ApJS, 94, 583
Gladders, M. D., & Yee, H. K. C. 2000, AJ, 120, 2148
Gonzalez, A. H., Zaritsky, D., Dalcanton, J. J., & Nelson, A. 2001, ApJS, 137, 117
Henry, J. P. 2000, ApJ, 534, 565

Henry, J. P., & Arnaud, K. A. 1991, ApJ, 372, 410
Henry, J. P., Gioia, I. M., Maccacaro, T., Morris, S. L., Stocke, J. T., & Wolter, A. 1992, ApJ, 386, 408
Hjorth, J., Oukbir, J., & van Kampen, E. 1998, MNRAS, 298, L1
Hoekstra, H., Yee, H. K. C., Gladders, M. D., Barrientos, L. F., Hall, P. B., & Infante, L. 2002, ApJ, 572, 55
Holder, G. P., Haiman, Z., & Mohr, J. 2001, ApJ, 560, L111
Holder, G. P., Mohr, J. J., Carlstrom, J. E., Evrard, A. E., & Leitch, E. M. 2000, ApJ, 544, 629
Horner, D. J., Mushotzky, R. F., & Scharf, C. A. 1999, ApJ, 520, 78
Jenkins, A., et al. 1998, ApJ, 499, 20
Jenkins, A., Frenk, C. S., White, S. D. M., Colberg, J. M., Cole, S., Evrard, A. E., Couchman, H. M. P., & Yoshida, N. 2001, MNRAS, 321, 372 (J01)
Jing, Y. P. 2000, ApJ, 535, 30
Kaiser, N. 1991, ApJ, 383, 104
Kay, S. T., Liddle, A. R., & Thomas, P. A. 2001, MNRAS, 325, 835
Kepner, J., Fan, X., Bahcall, N., Gunn, J., Lupton, R., & Xu, G. 1999, ApJ, 517, 78
Kerscher, M., Szapudi, I., & Szalay, A. S. 2000, ApJ, 535, L13
Kitayama, T., & Suto, Y. 1997, ApJ, 490, 557
Kneissl, R., Jones, M. E., Saunders, R., Eke, V. R., Lasenby, A. N., Grainge, K., & Cotter, G. 2001, MNRAS, 328, 783
Lacey, C., & Cole, S. 1994, MNRAS, 271, 676
Lahav, O., Rees, M. J., Lilje, P. B., & Primack, J. R. 1991, MNRAS, 251, 128
Lee, J., & Shandarin, S. 1999, ApJ, 517, L5
Lilje, P. B. 1992, ApJ, 386, L33
Lloyd-Davies, E. J., Ponman, T. J., & Cannon, D. B. 2000, MNRAS, 315, 689
Luppino, G., & Kaiser, N. 1997, ApJ, 475, 20
MacFarland, T., Couchman, H. M. P., Pearce, F. R., & Pichlmeier, J. 1998, NewA, 3, 687
Markevitch, M. 1998, ApJ, 504, 27
Mathiesen, B. F., & Evrard, A. E. 2001, ApJ, 546, 100
McNamara, B. R., Wise, M. W., David, L. P., Nulsen, P. E. J., & Sarazin, C. L. 2001, in Constructing the Universe with Clusters of Galaxies, ed. F. Durret & D. Gerbal (Paris: IAP), 89
Mellier, Y., & van Waerbeke, L. 2002, in Where's the Matter? Tracing Dark and Bright Matter with the New Generation of Large Scale Surveys, in press
Metzler, C. A., White, M., & Loken, C. 2001, ApJ, 547, 560
Mohr, J. J., & Evrard, A. E. 1997, ApJ, 491, 38
Mohr, J. J., Mathiesen, B., & Evrard, A. E. 1999, ApJ, 517, 627
Mohr, J. J., Reese, E. D., Ellingson, E., Lewis, A. D., & Evrard, A. E. 2000, ApJ, 544, 109
Moore, B., Governato, F., Quinn, T., Stadel, J., & Lake, G. 1998, ApJ, 499, L5
Mushotzky, R., & Scharf, C. A. 1997, ApJ, 482, L13
Navarro, J. F., Frenk, C. S., & White, S. D. M. 1996, ApJ, 462, 563
———. 1997, ApJ, 490, 493
Netterfield, C. B., et al. 2002, ApJ, 571, 604
Nevalainen, J., Markevitch, M., & Forman, W. 2000, ApJ, 536, 73
Nichol, R., et al. 2001, Mining the Sky, ed. A. J. Banday, S. Zaroubi, & M. Bartelmann (Heidelburg: Springer), 613
Ostrander, E. J., Nichol, R. C., Ratnatunga, K. U., & Griffiths, R. E. 1998, AJ, 116, 2644
Oukbir, J., & Blanchard, A. 1992, A&A, 262, L21
Outram, P. J., Hoyle, F., Shanks, T., Boyle, B. J., Croom, S. M., Loaring, N. S., Miller, L., & Smith, R. J. 2001, MNRAS, 328, 174
Padilla, N. D., & Baugh, C. M. 2002, MNRAS, 329, 431
Park, C., & Gott, J. R. 1991, ApJ, 378, 457
Pearce, F. R., & Couchman, H. M. P. 1997, NewA, 2, 411
Pen, U.-L. 1998, ApJ, 498, 60
Pierpaoli, E., Scott, D., & White, M. 2001, MNRAS, 325, 77 (PSW)
Postman, M., Lubin, L., Gunn, J. E., Oke, J. B., Hoessel, J. G., Schneider, D. P., & Christensen, J. A. 1996, AJ, 111, 615
Press, W. H., & Schechter, P. 1974, ApJ, 187, 425 (PS)
Pryke, C., Halverson, N. W., Leitch, E. M., Kovac, J., Carlstrom, J. E., Holzapfel, W. L., & Dragovan, M. 2002, ApJ, 568, 46
Romer, A. K., et al. 2000, ApJS, 126, 209
Romer, A. K., Viana, P. T. P., Liddle, A. R., & Mann, R. G. 2001, ApJ, 547, 594
Rosati, P., Della Ceca, R., Norman, C., & Giacconi, R. 1998, ApJ, 492, 21L
Sachs, L. 1982, Applied Statistics (New York: Springer)
Sadat, R., Blanchard, A., & Oukbir, J. 1998, A&A, 329, 21
Scharf, C. A., Jones, L. R., Ebeling, H., Perlman, E., Malkan, M., & Wegner, G. 1997, ApJ, 477, 79
Scodeggio, M., et al. 1999, A&AS, 137, 83
Seljak, U., & Zaldarriaga, M. 1996, ApJ, 469, 437
Sheldon, E. S., et al. 2001, ApJ, 554, 881
Sheth, R. K., & Tormen, G. 1999, MNRAS, 308, 119
Smith, D. R., Bernstein, G. M., Fischer, P., & Jarvis, M. 2001, ApJ, 551, 643
Springel, V., White, S. D. M., Tormen, G., & Kauffmann, G. 2001, MNRAS, 328, 726
Stanford, S. A., Elston, R., Eisenhardt, P., Spinrad, H., Stern, D., & Dey, A. 1997, AJ, 114, 2232
Stanford, S. A., Holden, B., Rosati, P., Tozzi, P., Borgani, S., Eisenhardt, P. R., & Spinrad, H. 2001, ApJ, 552, 504
Sunyaev, R., & Zeldovich, Y. B. 1972, Comments Astrophys. Space Phys., 4, 173
Szapudi, I., Colombi, S., Jenkins, A., & Colberg, J. 2000, MNRAS, 313, 725
Thomas, P. A., Muanwong, O., Pearce, F. R., Couchman, H. M. P., Edge, A. C., Jenkins, A., & Onuora, L. 2001, MNRAS, 324, 450
Tozzi, P., & Norman, C. 2001, ApJ, 546, 63
Tran, K.-V. H., Kelson, D. D., van Dokkum, P., Franx, M., Illingworth, G. D., & Magee, D. 1999, ApJ, 522, 39
Tucker, W., Blanco, P., Rappaport, S., David, L., Fabricant, D., Falco, E. E., Forman, W., Dressler, A., & Ramella, M. 1998, ApJ, 496, L5
Viana, P. T. P., & Liddle, A. R. 1996, MNRAS, 281, 323
———. 1999, MNRAS, 303, 535
Viklihnin, A., McNamara, B. R., Forman, W., Jones, C., Quintana, H., & Hornstrup, A. 1998, ApJ, 502, 558
Voit, G. M., Evrard, A. E., & Bryan, G. L. 2001, ApJ, 548, L123
White, D. A. 2000, MNRAS, 312, 663
White, M. 2001, A&A, 367, 27
White, M., van Warbeke, L., & Mackey, J. 2001, preprint (astro-ph/0111490)
White, S. D. M., Efstathiou, G., & Frenk, C. S. 1993, MNRAS, 262, 1023
Willick, J. A., Thompson, K. L., Mathiesen, B. F., Perlmutter, S., Knop, R. A., & Hill, G. J. 2001, PASP, 113, 658
Wilson, G., Kaiser, N., & Luppino, G. A. 2001, ApJ, 556, 601
Wu, X.-P., Xue, Y.-J., & Fang, L.-Z. 1999, ApJ, 524, 22
Yoshida, N. et al. 2001, MNRAS, 325, 803
Yoshikawa, K., Jing, Y. P., & Suto, Y. 2000, ApJ, 535, 593
Zaritsky, D., Nelson, A. E., Dalcanton, J. J., & Gonzalez, A. H. 1997, ApJ, 480, L91